CHALMERS
UNIVERSITY OF TECHNOLOGY

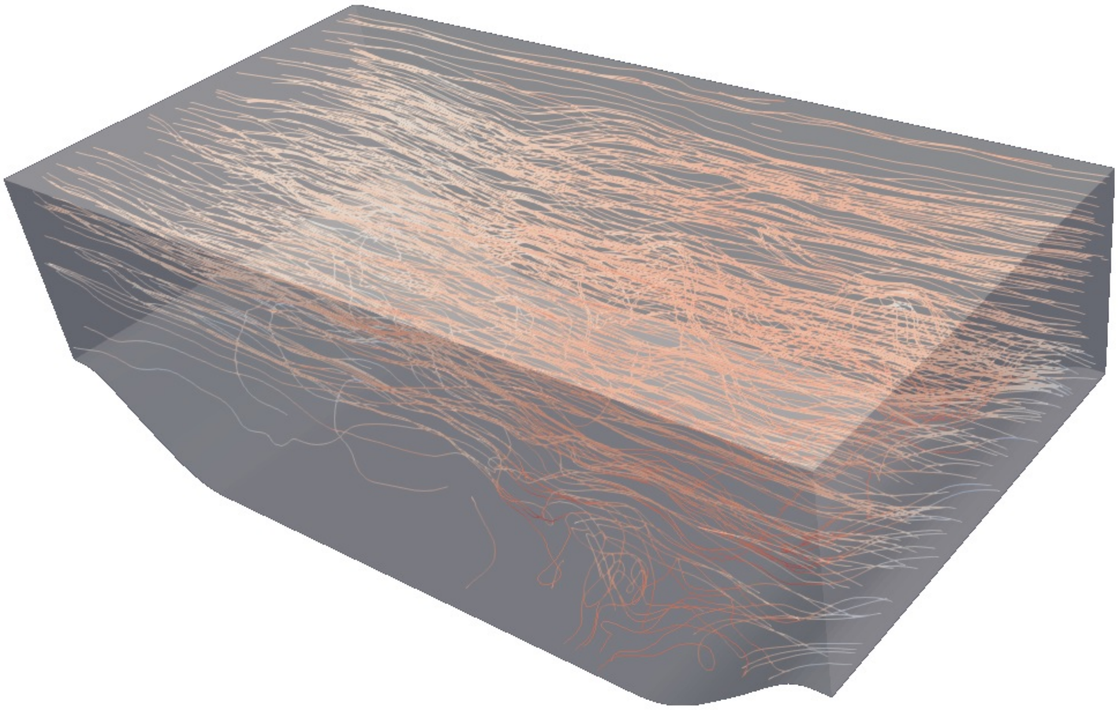

Evaluating the Performance of Wall-Modelled Large-Eddy Simulation on Unstructured Grids

Master's thesis in Naval Architecture and Ocean Engineering

MEHRAN JAVADI

Department of Mechanics and Maritime Sciences
CHALMERS UNIVERSITY OF TECHNOLOGY
Gothenburg, Sweden 2020

Master's thesis 2020:69

Evaluating the Performance of Wall-Modelled Large-Eddy Simulation on Unstructured Grids

Mehran Javadi

CHALMERS
UNIVERSITY OF TECHNOLOGY

Department of Mechanics and Maritime Sciences
Chalmers University of Technology
Gothenburg, Sweden 2020

Evaluating the Performance of Wall-Modelled Large-Eddy Simulation on Unstructured Grids

Mehran Javadi

Supervisor: Timofey Mukha, Department of Mechanics and Maritime Sciences
Examiner: Rickard Bensow, Department of Mechanics and Maritime Sciences

Master's Thesis 2020:69
Department of Mechanics and Maritime Sciences
Chalmers University of Technology
SE-412 96 Gothenburg
Telephone +46 31 772 1000

Cover: Computational domain for the flow over periodic hills.

Typeset in LaTeX
Printed by Chalmers Reproservice
Gothenburg, Sweden 2020

Evaluating the Performance of Wall-Modelled Large-Eddy Simulation on Unstructured Grids

Mehran Javadi
Department of Mechanics and Maritime Sciences
Chalmers University of Technology

Abstract

Large Eddy Simulation (LES) has become a promising CFD method for flows in which turbulence plays a dominant role such as many complex engineering systems. To contribute to further advances, in this work, the performance of Wall-Modelled LES on unstructured grids is evaluated. Periodically arranged hills geometry is a frequent experimental and numerical test case because of the possibility of studying important fluid phenomena. The importance of study of this flow arise from separation and reattachment points, and hence the whole flow is sensitive to the separation process. In this work, WMLES is used to investigate the properties of a separated flow in a periodic hill channel flow. The principal idea is to evaluate the sensitivity of the predicting accuracy to grid resolutions. To do that, three mesh types including triangle, polygon, and square prism meshes are employed in the study. Grid resolution has also been considered by using four grid sizes - different cell-to-cell distance - for each type of mesh. Twelve grids are used for the simulations and the results are judged by existing reference data. The results are included for skin friction and pressure coefficients, mean and vertical velocity, and kinetic energy profiles. The results illustrate that WMLES predict the flow features accurately. The statistical data elicited from the study illustrate a noticeable influence of grid topology on the results and prove that meshing strategy plays a key role in accurate prediction. Also, results illustrated a noticeable distinction in sensitivity between separation and reattachment points. Regarding this, the reattachment point is highly sensitive to the grid size.

Keywords: Computational Fluid Dynamics, WMLES, Unstructured grids, Accuracy, OpenFOAM.

Acknowledgements

I would first like to express my gratitude to my thesis advisor professor Rickard Bensow for all he have done not only for the current research, but also for all amazing courses which I passed during my master program. I learned a lot and benefited from your courses and I truly appreciate you and your time you spent helping me in many occasions. I also would like to say a special thank you to my patient, cool, and supportive supervisor, Timofey Mukha, who has supported me whenever I ran into a trouble spot or had a question about my research. I learned a lot from him and in such a short time like the thesis course, I certainly could not have completed the study without his help, guidance, and instructive view. I am extremely grateful for our friendly daily meeting and his personal support in my academic endeavours.
I own an special thanks to you, Mojgan and Siavash. I am really blessed to have you and I very much appreciate your support during this challenging time. Finally, I must express my very profound gratitude to my parents for providing me with unfailing support and continuous encouragement throughout my years of study and through the process of researching and writing this thesis. This accomplishment would not have been possible without them. Thank you.

Mehran Javadi, Gothenburg, September 2020

Contents

List of Figures

List of Tables

Nomenclature

Abbreviation

CFD	Computational fluid dynamics
LES	Large eddy simulation
WMLES	Wall-model large eddy simulation
WRLES	Wall-resolved large eddy simulation
RANS	Reynolds Average Navier Stokes
DNS	Direct numerical simulation
TBL	Turbulent boundary layer
SGS	Subgrid scale
SD	Spectral difference
WALE	Wall-adapting local eddy viscosity
DSM	Dynamic Smagorinsky model
CSM	Coherent structural model
AMI	Arbitrary mesh interface
CSM	Coherent structural model

General Notations

ρ	Density
ν	Kinematic velocity
u	Velocity
u, v, w	Velocity vectors
$\overline{u}_i$	Filtered velocity
u_τ	Friction velocity
μ	Molecular viscosity
g	Acceleration due to gravity
v	Vertical velocity
k	Turbulent kinetic energy
t	Time
$\overline{S}_{ij}$	Filtered tensor
$\overline{P}$	Filtered pressure
μ_{sgs}	Subgrid scale eddy viscosity
τ_{ij}	Stress tensor
C_s	Modelling constant
C_k	Kolmogorov constant
$\overline{\tau}_w$	Filtered wall shear stress
$\|U\|$	Wall-parallel velocity magnitude
L_x, L_y, L_z	Length, width, and height of the domain
y^+	Wall coordinate
u^+	Dimensionless velocity
C^+	Law of the wall's constant
h	Hill crest height
S	Cell surface area
d	Cell-to-cell distance
a	Cell edge size
Δ	Grid size

1

Introduction

1.1 Motivation for the study

Fluid flow behavior in many industrial systems has a large influence on the design process and system efficiency. Flow over a curved surface, involving turbulence and separating flow, occurs in numerous simple and complex engineering systems, such as a simple piping system to a high-tech turbogenerator or wind turbine blade's aerodynamic. For the flow over a curved surface, the separation point fluctuates spatially and temporally which results in a great influence on the downstream flow behavior.

In a complex computational domain, a meshing strategy is quite an important step in the simulation since a complex surface is more sensitive to the mesh resolution in comparison with the flat surface. Flow over a periodic hill arrangement is an attractive test benchmark to investigate the flow features. Numerous studies have been performed on the periodic hill arrangement over the past years using different numerical methods that made a source of data to compare.

In a wide range of Reynolds numbers, both experimental and numerical experiments were conducted over the periodic hill. Different numerical models were used such as RANS, LES, and DNS, but the most common methods are RANS and LES. Predictive ability is the main criteria which made LES method as an effective alternative in compare with RANS method [22]. The results from a previous study on the periodic hill show that the influence of grid size near the top wall has no impact on the flow features accuracy as much as the curved bottom wall and they can be resolved reasonably well by a relatively coarse mesh [2]. One approach to dealing with near-wall turbulence is wall modelling. Regarding this, the inner region of the boundary layers including small scales are modelled, whereas the outer region should be fully resolved by the computational grid. To increase the simulation accuracy, high-quality mesh in the outer layer of the turbulent boundary layer (TBL) is necessary. Moreover, structured mesh is the easiest way for the meshing of the domain, but in the case of complex domain flows, an unstructured grid works well. The performance of WMLES on unstructured grids is poorly explored compared with other CFD methods. The present study is aimed at evaluating grid topology impacts on WMLES performance. The computational domain with flow separation also is doubled the importance of the present study.

1.2 Literature review

Numerical simulation is widely being used for the design and development of engineering tools and systems. A more sophisticated coarse-grained flow model is used in large-eddy simulation (LES). The LES technique mostly being used in academic research but rarely in an industrial engineering design due to its large cost of handling turbulent boundary layers. There are many proposed solutions to the near-wall issue of LES and generally, the idea is modelling the turbulence in the inner part of the boundary layer. Hence, there is no need to resolve turbulent eddies in this area [1]. It can be argued that grid quality assessment for the simulation with the WMLES method is poorly considered and explored because of its rare use in a industrial applications. Also, the high cost of LES method for a turbulent flow with separation, not explored systematically at all.
The configuration of the periodic channel flow was originally proposed by Almeida and colleagues [9], and modified by Mellen, Fröhlich, and Rodi in 2000 [8]. In 2003, Temmerman and colleagues conducted numerical simulation on a same geometry using WMLES. In their work, simulations were performed at $Re = 10595$ and in different subgrid scale (SGS) models and wall-functions. The results show that the flow pattern, specifically in separation zone, is more sensitive to the wall model than the SGS model. In 2005, Fröhlich et al. investigated the performance LES at $Re = 10595$ using two different second order finite volume discretizations. In their research, they used two subgrid scale models, the dynamic Smagorinsky model and the 'wall-adapted local eddy-viscosity' model. In another work, Breuer et al. [10] performed a direct numerical simulation (DNS) and wall-resolved LES on the periodic hill configuration and compared the results with the experimental data. The Reynolds numbers were 5600 and 10595 for the DNS and WRLES, respectively. In 2014, separating flow in a channel with streamwise periodic constrictions was investigated using DNS, LES, and WMLES by Balakumar and colleagues. In this work, they investigated the mean velocity profiles and separation/reattachment points for all three CFD methods. The results show that the high-resolution DNS has very good agreement with the reference experiment. Despite the very coarse resolution, the results from WMLES with three different wall models are comparable to those from the DNS and the experiment [17]. In 2019, Xavier and Paola, studied the requirements of large-eddy simulation on flow with separation using a channel with streamwise-periodic constrictions. They studied the mesh resolution impact on reattachment point and energy spectra. The results showed that the delicate flow details in this study, hardly resolved on coarse grids at low Reynolds numbers[2].
In 2017, Krank and colleagues extended an approach of wall modeling via function enrichment to detached-eddy simulation. The aim of their study was using coarse cells in the near wall region by the velocity profile in the sublayer and log layer. Flow over periodic hills shows the superiority of prediction accuracy compared to an equilibrium wall model under separated flow conditions [4].
The combination of the high-order unstructured Spectral Difference (SD) spatial discretization scheme with SGS modeling for WMLES was investigated by Lodato and colleagues, 2014 [5]. In this study, two different wall-models were tested, a classical three-layers wall-function and a more general formulation to account for

the pressure gradient in more complex configurations. The mixed scale-similarity SGS model was used in the entire computational domain without any particular adjustment inside the wall-modeled region and the results showed noticeable improvements in the simulation result.
The role of unstructured mesh on LES studied by Boudier and Staffelbach, 2008. In this study that performed on a domain corresponding to a sector of a realistic helicopter chamber, three grid resolution from 1.2 to 44 million elements were used for LES. Results showed that the mean temperature, reaction rate, and velocity fields are almost insensitive to the grid size. However, the RMS fields of the resolved velocity was independent of the mesh [18].

1.3 Present work

In the present study, the predictive accuracy of wall-modelled LES on unstructured grids with different cell topologies is evaluated. Figure 1.1 shows a periodic hill as the test case in this work.

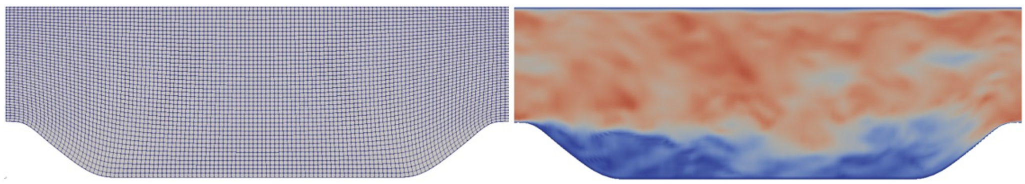

Figure 1.1: Periodic hill test case.

The configuration of the flow in a periodic channel is used to evaluate the WMLES performance on unstructured grids by focusing on prediction of separation and re-attachment points. To investigate the WMLES method on unstructured grid performance, the flow features including wall shear stress, mean and vertical velocity profiles, kinetic energy, and turbulence intensity are assessed. It should be noted that the main focus is on the bottom side where the boundary layer flow is very challenging for wall functions and modeling of near-wall effects.
The goal of the study is to evaluate the LES method on unstructured grids with three different mesh topology including square mesh, triangle mesh, and polygon mesh. To that end, Pointwise meshing algorithms and STAR-CCM+ have been employed for grid construction, whereas the open-source CFD software OpenFOAM is used for the simulation. In what follows, mathematical formulation of simulation discussed in chapter 2. Chapter 3 discussed the computational domain set-up, geometry features, and flow conditions. Meshing strategy and configurations discussed in chapter 4. Chapter 5 discusses the outputs of the simulations, and finally, the study concluded in chapter 6.

2

Simulation Methodology

This chapter is devoted to the basic mathematical formulation of the study. Regarding this, the flow configuration discussing all equations needed to solve the WMLES includes the boundary conditions in a wall-bounded domain. This chapter including the details of the wall model, the SGS model and the numerical methods.

2.1 Introduction to LES

Large-Eddy Simulation (LES) is closely related to DNS, but has numerous unique features which are particular to LES. Suppose a CFD simulation perform a DNS, using coarser grid is necessary if the number of required grids exceeds the capacity of the available computer. These coarser grids are able to solve the larger eddies in the turbulent flow however, the smaller eddies - smaller that one or two cells - should be modelled. Small eddies require a so-called subgrid-scale (SGS) model. Modelling only the small eddies while the large eddies resolve by coarser grids is an advantage of LES approach compared to methods based on RANS equations. The CFD simulation using RANS shows that there are some difficulties when this approach is applied to rotational flow, complex flow, curved surfaces or compression. Also, LES gives access to the dominant unsteady motion so that it can, for instance, be applied to fluid-structure coupling [15].

2.2 LES Governing Equations

To formulate the 3D unsteady governing equations for large eddies, a low pass spatial filter is applied. In implicit filtering, there is no need to apply a filter to the instantaneous equation explicitly as the finite volume method is employed to solve the instantaneous governing equations. Hence, the equations are integrated over control volumes, equivalent to convolution with a top-hat filter. The Navier–Stokes equations for the resolved velocity $\bar{u}_i$ and the filtered pressure $\overline{p}$ are:

$$\frac{\partial \bar{u}_i}{\partial x_i} = 0 \tag{2.1}$$

$$\frac{\partial(\bar{u}_i)}{\partial t} + \frac{\partial(\bar{u}_i \bar{u}_j)}{\partial x_j} = -\frac{1}{\rho}\frac{\partial \bar{p}}{\partial x_i} + \frac{\partial(2\nu \bar{S_{ij}})}{\partial x_j} - \frac{1}{\rho}\frac{\partial(\tau_{ij})}{\partial x_j} + f \tag{2.2}$$

where the filtered strain-rate tensor is:

$$\overline{S}_{ij} = \frac{1}{2}(\frac{\partial \overline{u}_i}{\partial x_j} + \frac{\partial \overline{u}_j}{\partial x_i}) \tag{2.3}$$

The stress tensor, τ_{ij}, results from the unresolved subgrid-scale contributions and is:

$$\tau_{ij} = \overline{u_i u_j} - \overline{u}_i \overline{u}_j \tag{2.4}$$

where ν is molecular viscosity, $\overline{S}_{ij}$ is filtered tensor. The flow in the present stream-wise periodic configuration is driven by a pressure gradient, here represented through the volume force f which is constant in space.

2.3 Subgrid-Scale Modelling

In LES, missing turbulent motions need to be modelled particularly near the wall. The main feature of the LES method is subgrid-scale modelling. In three dimensional turbulent flow, energy cascades should translate from large scales to the small ones. Hence, the major task of SGS is to ensure correct energy transport.
There are many developed SGS models the majority of them following Boussinesq's hypothesis to model the SGS stress tensor. The WALE model is the anisotropic part of the SGS term as:

$$\frac{1}{\rho}(\tau_{ij} - \frac{1}{3}\delta_{ij}\tau_{kk}) = -2\nu_t \bar{S}_{ij} \tag{2.5}$$

where δ_{ij} is the Kronecker delta, τ_{kk} is lumped into a modified pressure and considered negligible, but differing in the way the eddy viscosity, ν_t, is determined.
The WALE model is based on the symmetric part of the square of velocity-gradient tensor, $g_{ij} = \frac{\partial u_i}{\partial x_j}$.

$$\bar{G}_{ij} = \frac{1}{2}(\bar{g}_{ik}\bar{g}_{kj} + \bar{g}_{jk}\bar{g}_{ki}) \tag{2.6}$$

and its traceless part is

$$\bar{G}^a_{ij} = \bar{G}_{ij} - \frac{1}{3}\delta_{ij}\bar{G}_{kk} \tag{2.7}$$

Hence the eddy viscosity is

$$\nu_t = C_w \Delta^2 \frac{(\sqrt{|\bar{G}^a|})^6}{|\bar{S}|^5 + \sqrt{(|\bar{G}^a|)^5}} \tag{2.8}$$

where Δ is the grid size and $C_w$is a model constant. In case of pure shear stress, $|\bar{G}^a| = 0$ and hence $\nu_t = 0$.

2.4 Wall Modelling

The most challenging issue for many complex CFD domains with turbulent flow is resolving the inner layer of the turbulent boundary layer (TBL). The number of grid points required for the wall-resolved LES in a turbulent flow and close to the wall is significantly effective on the simulation result accuracy because of the importance of the TBL inner layer simulation. The inner length scale of TBL is δ_v. The required number of grid cells in TBL depends on the Reynolds number directly. Wall-stress modelling and hybrid LES/RANS are two major WMLES approaches [3].

2.4.1 Taxonomy of WMLES methods

Two common methodologies for the near wall modelling are wall-stress modelling and hybrid LES/RANS. The main difference between methods is caused by the definition of the extend of the LES domain. In this study wall-stress modelling is used.

2.4.1.1 Wall-stress models

To investigate the wall-shear stress as a critical term of WMLES method performance assessment, a wall-law approximation is needed at computational node close to the wall to return the correct instantaneous wall-shear stress corresponding to the mean velocity. Fig. 2.1 shows a schematic of the wall-stress modelling approach. In wall-stress modelling, the target region is the whole region close to the wall and inner layer. Hence, defining a correct boundary condition at the wall for the LES equations is the main strategy. Filtered wall shear stress , $\bar{\tau}_w$, is the critical parameter to assess the wall-stress method. To predict the value of $\bar{\tau}_w$, a single point at some distance from the surface can be selected that LES solution is applied at this point.

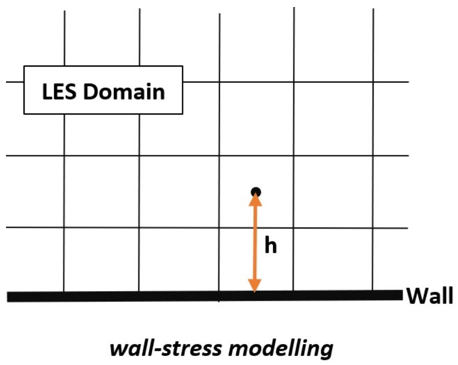

Figure 2.1: Schematic of two wall-modelling approaches include wall-stress modelling.

In wall-stress modelling, a local cartesian coordinate system can be defined such that the domain wall is in line with $x_1 - x_3$ plane and x_2 points is aligned with the mean wall-parallel components of velocity. The effect of wall shear stress, τ_{ij}, enters the LES momentum equation via the following term:

$$\frac{1}{\rho}\frac{\partial \tau_{ij}}{\partial x_j} \tag{2.9}$$

where $\frac{1}{\rho}\tau_{ij} = 2\nu\bar{S_{ij}}$. By considering a finite volume cell with a face of size S_w adjacent to the wall and integrating $\frac{\partial \tau_{ij}}{\partial x_j}$ over the volume of the cell and using Gauss-Ostrogradsky theorem results in an integral over the cell surface, it can be written as:

$$\int_{S_w} \tau_{ij} n_j dS = -\int_{S_w} \tau_{i2} dS \approx \bar{\tau}_{w,i2} S_w \tag{2.10}$$

where $(i = 1, 3)$ illustrate two wall parallel components of the filtered wall shear stress vector $\bar{\tau_w}$ and n is the surface normal. Note that in WMLES method the size of grid is too coarse to resolve the wall-normal velocity gradient and $\bar{\tau}_w$ has to supplied by a wall model instead [3].

2.4.2 Law of the wall

The wall model employed in this study to find the wall shear stress, $\bar{\tau}_w$, is Spalding's law. Based on Prandtl (1933), the mean velocity, u, near the smooth wall is depend on density and viscosity of the fluid. The shear stress at the wall and on the distance from the wall are τ_w and y, respectively. Thus there is a functional relationship:

$$u = u(\rho, \nu, \tau_w, y) \tag{2.11}$$

By introducing $u^+ = u/u_\tau$ and $y^+ = yu_\tau/\nu$, then the law of the wall is:

$$u^+ = \frac{1}{k} ln(y^+) + C^+ \tag{2.12}$$

in which y^+ is the wall coordinate, u^+ is the dimensionless velocity, C^+ is a constant, and k is the Von Kármán constant. The ν is kinematic viscosity and u_τ is the friction velocity or shear velocity. The u_τ the shear velocity can be define as:

$$u_\tau = \sqrt{\frac{\tau_w}{\rho}} \tag{2.13}$$

In this work, an algebraic wall-stress model based on Spalding's formulation is used.

$$y^+ = f(u^+) = u^+ + A[e^{ku^+} - 1 - ku^+ - \frac{(ku^+)^2}{2} - \frac{(ku^+)^3}{6} - \frac{(ku^+)^4}{24}] \tag{2.14}$$

where $A = e^{-kC^+} = 0.1108$, $k = 0.4$, and $C^+ = 5.5$. The assumption is that a law of wall model is valid for mean velocity [19].

3

Computational Domain Setup

3.1 Geometry

The present computational benchmark has been selected for investigation of structured and unstructured grid topology and wall-modelling. The benchmark is highly important because of separation on a smooth curved surface. The chosen computational domain was introduced by Mellen, Frohlich, and Rodi (2000). The geometry characteristics such as short crest-to-crest distance and wavy-terrain geometry can provide all necessary needs to investigate the WMLES method performance on the result accuracy [8]. Figure 3.1 shows the test case. The geometry consists of two hill crests of height h at both ends. The length (L_x), width (L_z), and height (L_y) of the domain are $9.0h$, $4.5h$, and $2.035h$, respectively. Table 3.1 shows the domain dimensions and properties.
To obtain reliable results, the spanwise extent is highly important and two-point correlation in the spanwise direction must decay small values in the half-width of the domain size. Based on [8], and domain with the reference data, a spanwise extension of the computational domain of $L_z = 4.5h$ is used.

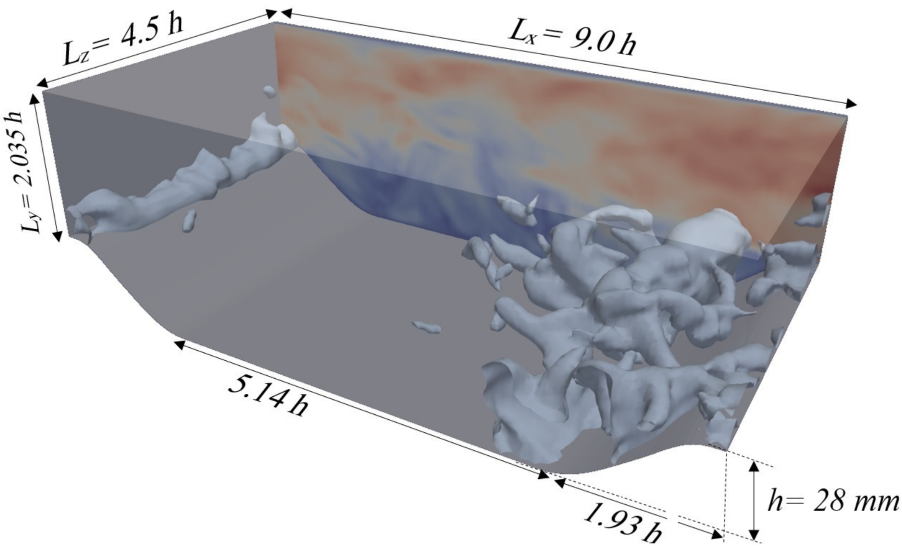

Figure 3.1: Schematic of the computational benchmark.

Table 3.1: Periodic hill geometry dimensions.

Parameter	Ratio	Dimension (mm)
Length (L_x)	9.0h	252
Width (L_z)	4.5h	126
Height (L_y)	2.035h	56.98
Crest height (h)	h	28
Midsection	5.14h	143.92
Curved surface length	1.93h	54.04

3.2 Flow Conditions

Due to the shape of the channel, the flow is fully turbulent. The flow pattern has a periodicity along the domain with a sufficient distance between two consecutive crests. Moreover, the averaging along the span can be used to improve the statistical convergence.
In the present benchmark, periodic boundary conditions are applied for the domain in the spanwise and streamwise directions. There is also no need for a specification of inflow conditions because of streamwise periodicity. The rate of required flow imposed through a pressure-forcing is constant and adjusted in time. Hence, the Reynolds number is invariant across the entire range of simulation, while pressure gradient can vary a bit in time. In this geometry, with the length of $9h$, the reattachment point is not enforced close to the hill crest and the structure of the separation region is highly sensitive to the mesh topology and the modelling details.
The Reynolds number has been chosen based on the hill height, h, and bulk flow velocity over the hill. The laminar viscosity is set to achieve the target Reynolds numbers. The inlet velocity is 1 m/s and at the bottom and top side considered by solid walls and no-slip condition is used in this areas.

$$Re = \frac{U_b h}{\nu} = \frac{1 \times 0.028}{2.65 \times 10^{-6}} = 10565 \tag{3.1}$$

$$U_b = \frac{1}{3.035h} \int_h^{3.035h} u(y) dy \tag{3.2}$$

Despite the high Reynolds number needed for a investigation the influence of wall-function on the flow conditions, the Reynolds number has been chosen as a low value to a level allowing almost fully resolved simulation and reasonable cost.

3.3 Initial and Boundary Conditions

To test the wall model a great variation of y^+ across the near wall grid plane is a particular advantage of the domain with a separated flow. The hill geometry has patches which connect the regions through the arbitrary mesh interface (AMI). Patches maps values between two sides of the domain. Following is the Cyclic boundary condition which is applied for the domain:

- Coupling condition between a pair of patches
- Faces value are determined by linear interpolation between cell values

Boundary condition has been defined in the mesh creation process and is the last step of meshing before exporting the meshed domain. Cyclic boundary condition is defined by boundary type cyclic. cyclicAMI is a coupling condition between a pair of patches that share the same outer bounds, but whose inner construction may be dissimilar. The difference between cyclic and cyclicAMI is the cyclic connects two equal meshes. Boundary condition cyclic requires the same size, same topology, same elements and even the same indexing order of faces [21].
Considering the hill geometry, there are different patches including inlet, outlet, and walls. Follow is the velocity and pressure fields initial conditions.

Patch	**Velocity Condition**
Inlet	cyclicAMI
Outlet	cyclicAMI
left	cyclicAMI
right	cyclicAMI
bottomWall	noslip
topWall	noslip

Patch	**Pressure Condition**
Inlet	cyclicAMI
Outlet	cyclicAMI
left	cyclicAMI
right	cyclicAMI
bottomWall	zeroGradient
topWall	zeroGradient

4
Meshing

This chapter discusses the mesh generation methodology for all cases. In this study, both structured and unstructured meshes are used to make comparable results to the reference data. Meshing algorithms in Pointwise V18.3 and STAR-CCM+ are employed to generate the structured and unstructured meshes, respectively. The following will explain mesh configurations and strategy applied to create the meshes.

4.1 Introduction

Still it is a big and challenging question for CFD engineers on how to choose an ideal type of mesh. Less control ability of the structured mesh in comparison with unstructured mesh is a common argue between CFD engineers. Regarding this, several factors have confirmed this idea [12]:

- **Resolution:** Fluid phenomena have some milder gradients along the domain and strong gradients in the transverse direction such as boundary and shear layers. It is difficult to generate accurate CFD results using tetrahedral, while hexahedra grids with high aspect ratio can easily generate.
- **Alignment:** Grid alignment with the predominant flow direction has a great influence on the CFD solver convergence. In a structured mesh, grids line follow the contours of the geometry, whereas there is no such alignment in an unstructured mesh.
- **Merge domain's part:** In many complex industrial systems, numerous parts must simulated as a computational domain. Unstructured grids are more flexible to merge parts to each other rather than structured one.
- **Meshing experience:** Structured mesh needs to be controlled particularly in case of complex domain or domain with curved surfaces, while there is no need for a long time experience to create an unstructured grid.

Regarding these factors, unstructured grid is widely used in simulations. This section discussed the mesh generation strategy for structured and unstructured grid types. To do that, different mesh types have been considered.

4.2 CAD Generation

To create a computational domain, an accurate CAD geometry is needed which must be as accurate as the real object or system. In 3D computational domain, like the current one, an accurate 3D CAD model data are the function and starting point of the computational simulation.

In the present work, the CAD domain has been created based on Almeida's domain dimensions [9]. Data are including the general dimensions in x, y, and z directions. To create the geometry, the Solidworks CAD software has been used with two main principles:

- Direct use of original geometry
- Domain geometry generated by Solidworks has a great compatibility with mesh generating options such as Pointwise and STAR-CCM+ and does not set constraints on meshing.

4.3 Meshing Strategy

Three types of meshes including *Triangle*, *Polygon*, and *Square* have been employed in the domain. Since the resolution of the mesh is one of the key factor of simulation accuracy, four different grid sizes have been considered. For structured meshing in Pointwise, as a first step, the total length of the domain divided by the number of cells along the x-direction and then based on cell size in x-direction, the number of cells in z and y directions is calculated. Table 4.1 shows the relation between cell surface area (S), edge size (a), and distance between two cell centers (d). Table 4.2 shows the cell sizes in x-direction and the number of cells along the domain. In this table and as it can be seen from fig. 4.1, the distance between two neighbour cell centers or the average cell-to-cell distance is defined as d [3].

Table 4.1: The relation between cell surface area (S), edge size (a), and distance between two cell centers (d).

Mesh Type	$S(a)$	$S(d)$	$d(a)$
Triangle	$\sqrt{3}/4a^2 \approx 0.43a^2$	$3\sqrt{3}/4d^2 \approx 1.30d^2$	$\sqrt{3}/3a \approx 0.57a$
Square	a^2	d^2	a
Polygon	$3\sqrt{3}/2a^2 \approx 2.60a^2$	$\sqrt{3}/2d^2 \approx 0.87d^2$	$\sqrt{3}a \approx 1.73a$

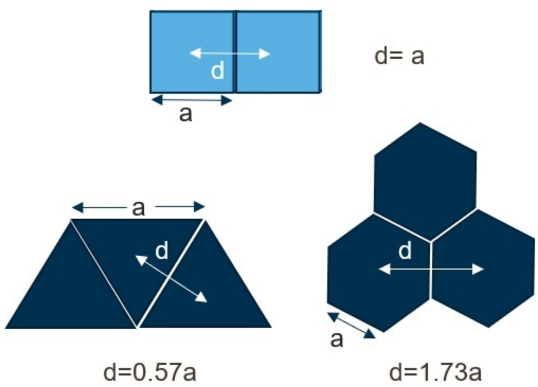

Figure 4.1: Cell-to-cell distance relationships for three types of mesh.

From the table 4.2, d_4 and d_1 represent the finest and coarsest structured meshes, respectively. Due to the special shape of the domain, cells in the midsection are cube while the cells in both ends of the domain are hexahedral and more denser compare to the midsection.

Table 4.2: Relationship between cell size and number of grids along the domain with structured mesh.

Quantity	Cell size (mm)	Number of cells in x-direction
d_4	1.432	176
d_3	2	126
d_2	2.25	112
d_1	2.625	96

To generate the polygone and triangle meshes, STAR-CCM+ software is applied. Hence, the domain has been divided into the same cell-to-cell distance. The "direct mesh" is the strategy to create grids with the same size along the vertical direction of the domain (y-direction). First, the bottom surface is meshed in such a way, that the average distance between the cell centres, d, is defined as base size. Then, surface mesh extruded along the wall-normal direction into the top wall of the domain. The total number of layers generated by extrusion depends on cell centres distance, d. Note that for both polygon and triangle mesh with the same d, the number of extrusion layers are same. Regarding this, the number of layers for $Poly_4$, $Poly_3$, $Poly_2$, and $Poly_1$ are 40, 29, 25, and 22, respectively.

4.4 Mesh Configurations

In this work, twelve mesh configurations are used to evaluate the influence of mesh topology on the simulation result. Figure 4.2 shows all mesh candidates for the study. A critical step in mesh generation procedure is the bottom surface mesh generation. To have comparable results, the accurate distance between two neighbor cell centers, d, is essential.

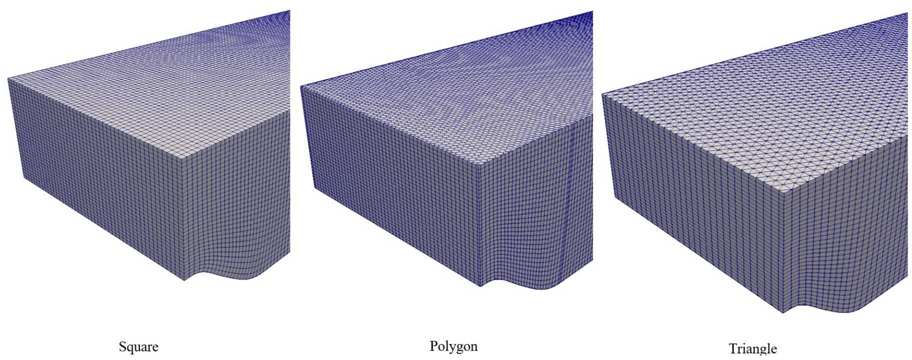

Figure 4.2: Schematic of three mesh candidates include triangle, polygon, and square mesh.

Table 4.3 shows the three types of mesh and four different mesh resolutions for each. Mesh resolution is based on the cell center to its neighbor cell center and represented

by d. d_4 and d_1 demonstrate the finest and coarse meshes, respectively. Regarding this, $d_4 = 1.432$ has been applied to generate the finest mesh, and $d_1 = 2.625$ has been applied to create the most coarse mesh and $d_3 = 2$ and $d_2 = 2.25$ are two selected grid sizes in between.
In normal and spanwise directions, grid resolutions are used with uniformly spaced grid and The cell-to-cell distance in every direction is d. The wall-normal distance of the sampling point used by the wall model is $d/2$ since the first cell is the sample.

Table 4.3: The number of cells for the cases with different grid topology.

Mesh Type	**Case name**	**cell-to-cell distance(mm)**	**Number of cells ($\times 10^3$)**
Triangle	Tri_4	d_4	655
	Tri_3	d_3	238
	Tri_2	d_2	208
	Tri_1	d_1	117
Polygon	$Poly_4$	d_4	998
	$Poly_3$	d_3	414
	$Poly_2$	d_2	301
	$Poly_1$	d_1	179
Square	Sq_4	d_4	898
	Sq_3	d_3	325
	Sq_2	d_2	225
	Sq_1	d_1	138

Depending on the elements, the number of cells is different along the domain. In the y-direction, the number of layers is same for all types of mesh with same d size. Hence, the number of grids in all directions should be calculated. Fig. 4.3 shows a schematic of the domain with triangle mesh in three different views.

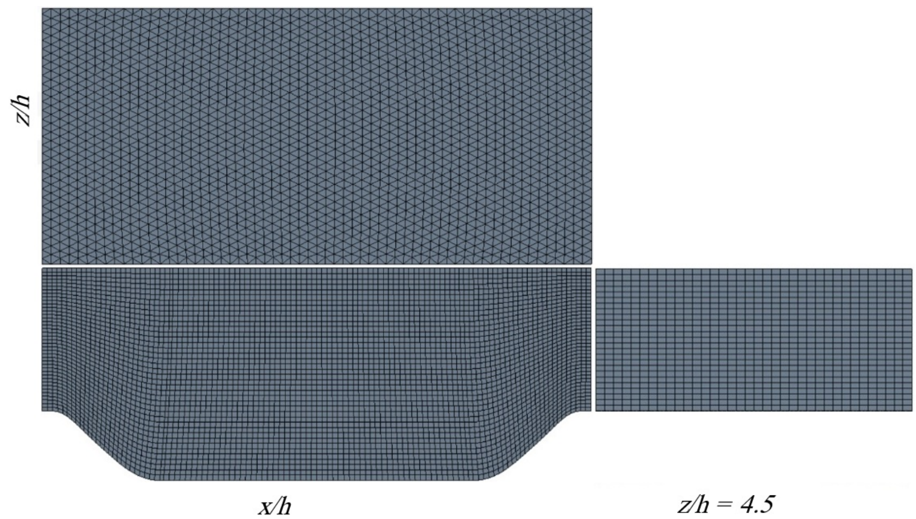

Figure 4.3: Schematic of mesh topology of the triangle mesh, (d_2).

5
Results

This section presents a set of comparisons between models with different grid topology and reference data. The reference data is a wall-resolved LES previously conducted by colleagues at Chalmers University of Technology which shows good agreement with DNS/LES results previously reported by Frölich [6]. An overall view of the flow pattern in the channel is conveyed in Fig.5.1 which shows streamfunction contour. In this section, substantial differences between models is evaluated and dependency of simulation accuracy to grid topology is investigated. To make a comparable results for all cases, Fig. 5.1 shows the certain location of profiles at $x/h = 0.05, 0.5, 2, 4, 6, 7$. These locations are scaled up by hill height, h, and then all profiles and data have been compared in this scale.

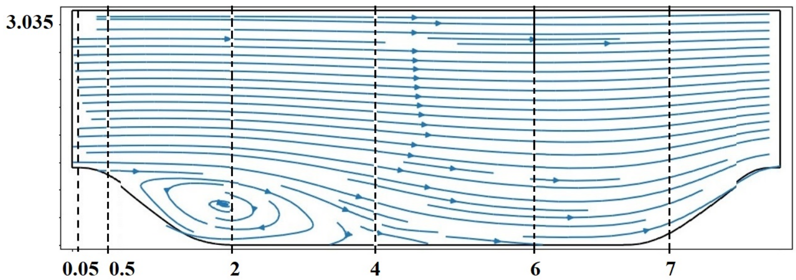

Figure 5.1: Streamlines of the average flow and dashed lines show the locations $x/h = 0.05, 0.5, 2, 4, 6, 7$ where analysis has been performed.

5.1 Pressure and skin friction coefficients

To investigate the flow behavior in the channel, there are some major global flow characteristics like pressure and skin friction coefficients that can express changes in the flow pattern due to changes in the domain properties. It means that different mesh typologies have a direct influence on the flow features.

5.1.1 Pressure coefficient

Fig. 5.2 shows the normalized distribution pressure along the top and bottom surfaces of the domain. It can be seen that, the pressure coefficient on the bottom wall has some fluctuations over the first one-third length of the domain including the recirculation zone. In the downstream zone the pressure value increases gradually and reaches its maximum value before the second hill. The top wall of the domain has experienced a turning point in the same place where the bottom wall pressure start to increase.

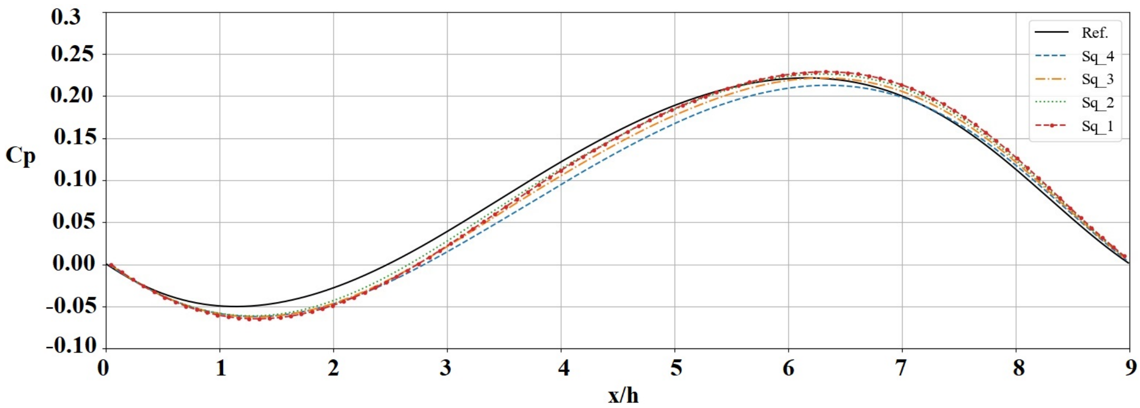

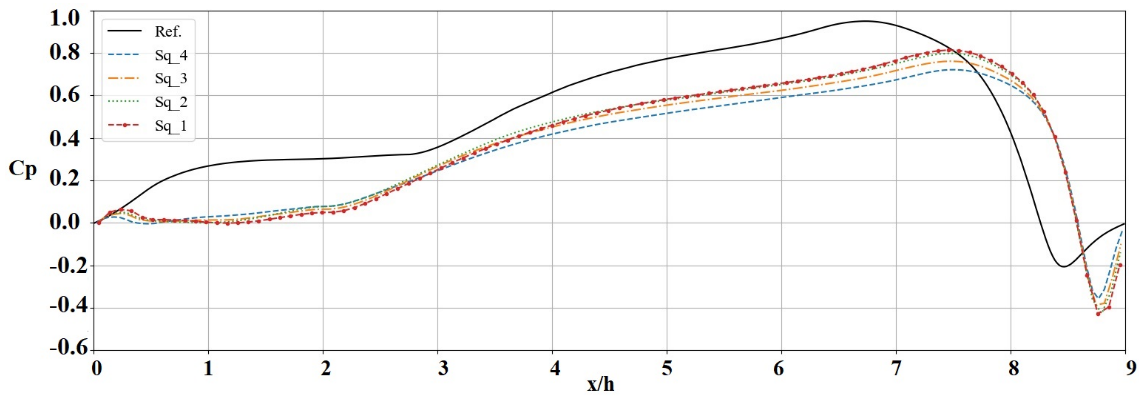

Figure 5.2: Pressure coefficient along the top and bottom wall for the domain with square mesh.

Fig. 5.2 also shows that the square meshes have a good agreement for almost all mesh sizes, while there is some deviation exists from the reference case. The top wall data shows more agreement between square cases in compare with reference case.

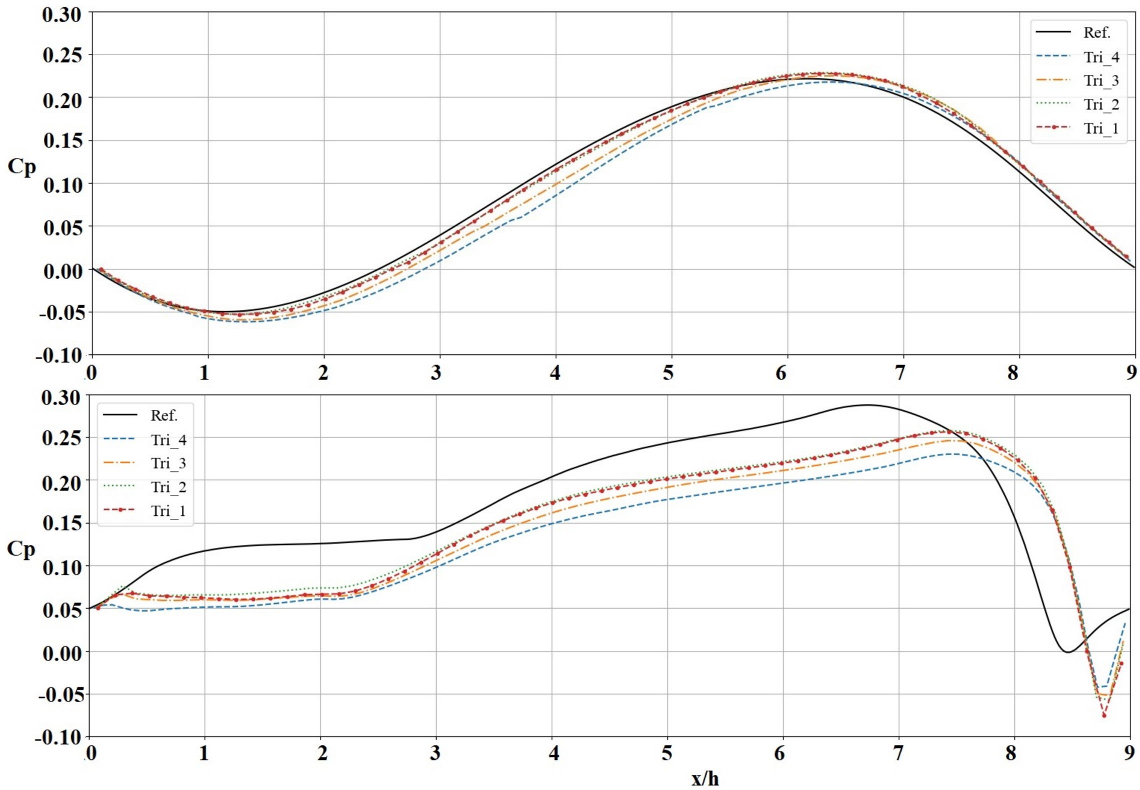

Figure 5.3: Pressure coefficient along the top and bottom wall for the domain with triangle mesh.

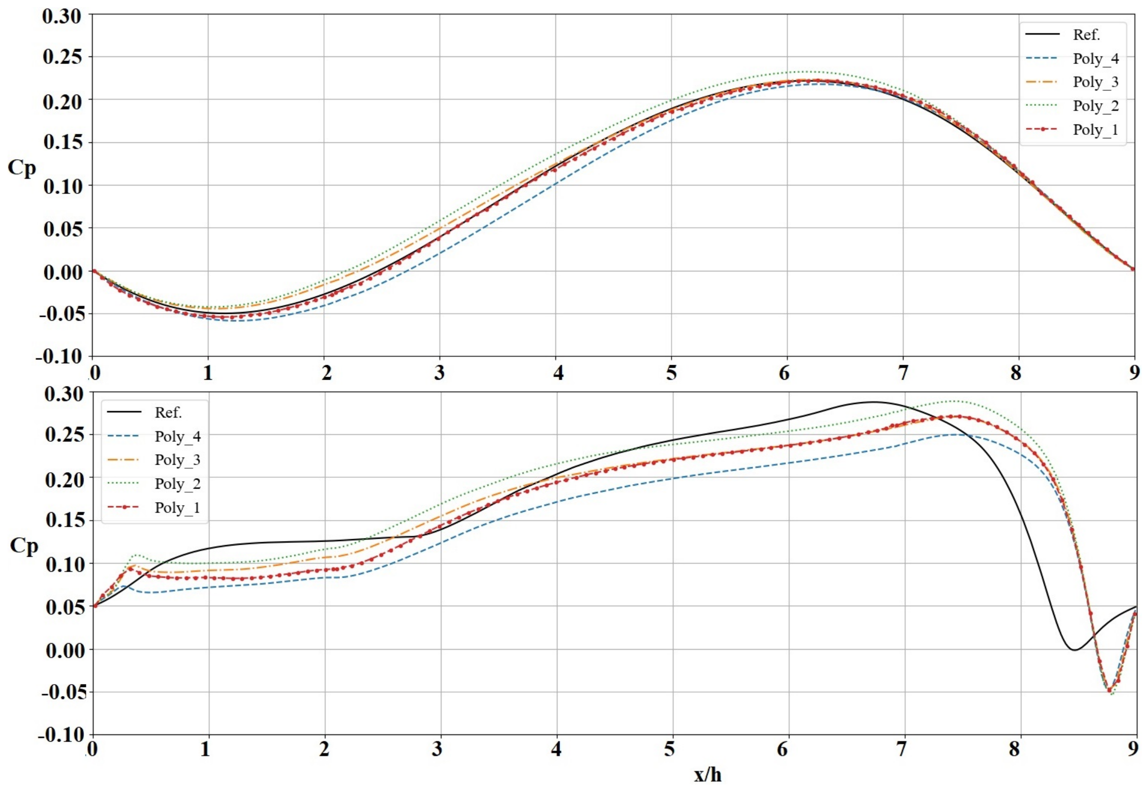

Figure 5.4: Pressure coefficient along the top and bottom wall for the domain with polygon mesh.

Fig. 5.3 and 5.4 show the C_p graphs for triangle and polygon meshes and indicates that the general trend is almost similar to the square meshes. From the figures, Tri_1 and $Poly_2$ are closer to the reference case. Figures also highlighted more agreement with the reference case in comparison with square meshes. It can be seen that the grid resolution for the polygon mesh has a significant influence on the C_p values.

5.1.2 Skin friction coefficient

Fig. 5.5 shows the skin-friction coefficients for all three types of meshes with the finest mesh. The skin-friction distribution on the top and bottom walls indicate a rather irregular, geometry-induced variation of the near-wall velocity used by the wall model for predicting the wall shear stress. Looking at the figure, it can be seen that there are two points on the bottom wall where the skin-friction coefficient is equal to zero. These points indicate the separation and reattachment points. The separation point occurs close to the crest of the hill, ($x/h = 0.3515$), and reattachment point is occur in the middle of the domain, ($x/h = 4.49$).

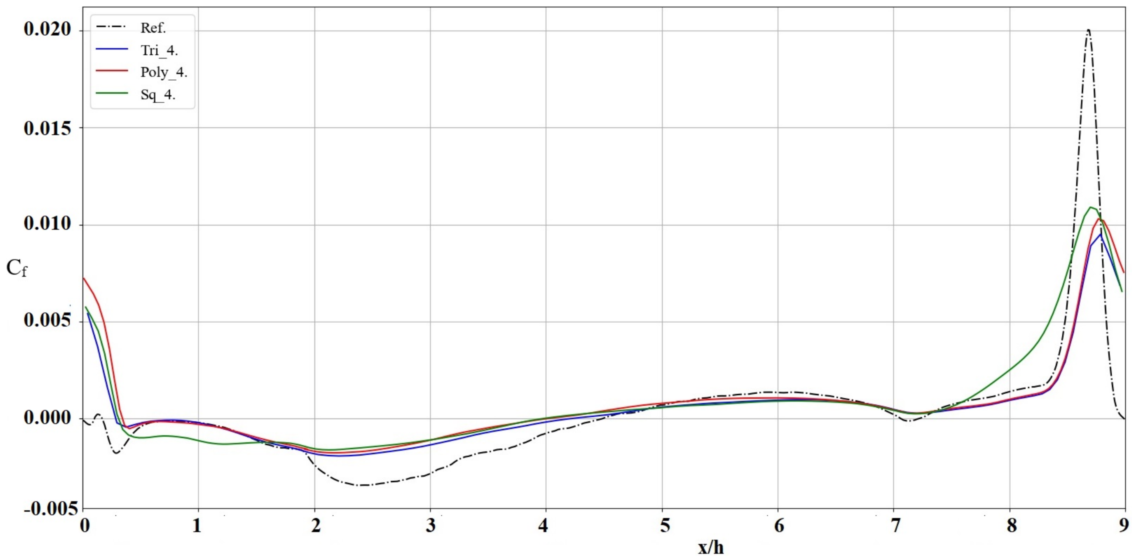

Figure 5.5: Skin friction coefficient for all fine meshes.

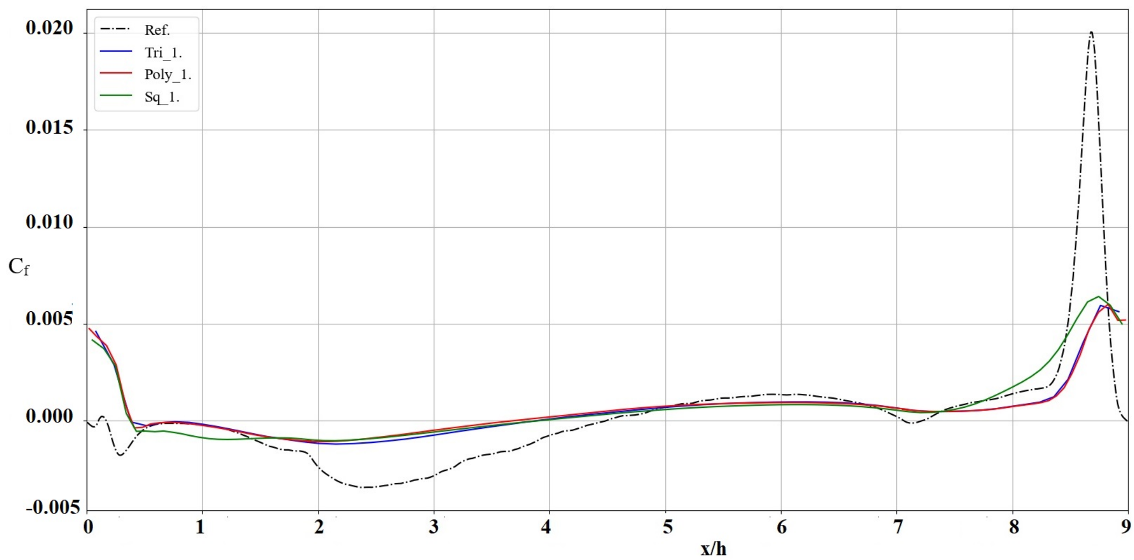

Figure 5.6: Skin friction coefficient for all coarse meshes.

Fig. 5.6 shows the skin friction coefficients for all three types of mesh with coarse grid. It can be seen that results are close to each other, however, the reattachment point for coarse meshes are occur a bit earlier than reference data. Reattachment point on coarse meshes also have more deviation from the reference data comparing with fine meshes.

5.2 Velocity and kinetic energy profiles

This section discusses mean and vertical velocities and kinetic energy profiles. Three main zones including separation, reattachment, and recirculation zones focused. In the separation point, boundary layer detaches from the surface and recirculation is formed and after that, reattachment point occurs.

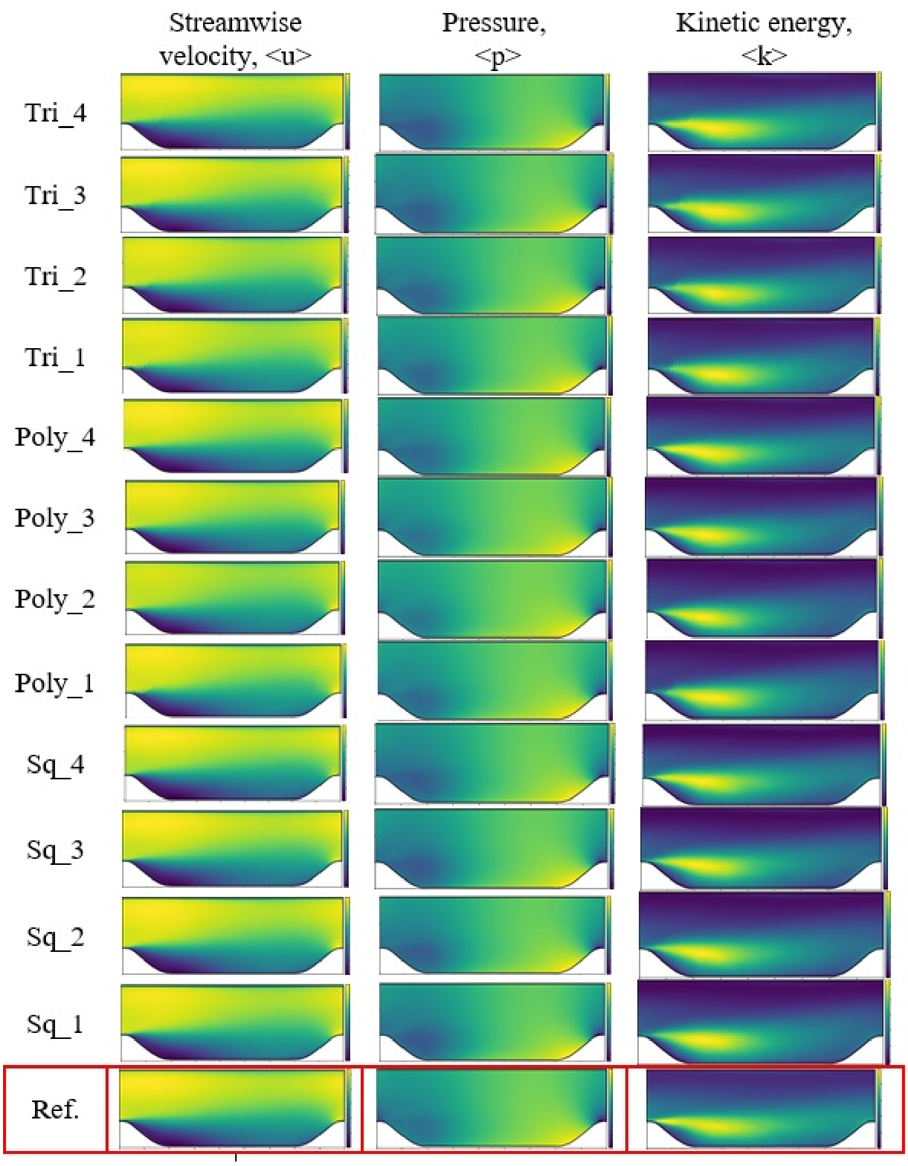

Figure 5.7: Velocity, pressure, and kinetic energy contours.

The velocity and kinetic energy profiles are elicited in seven certain locations, $x/h = 0.05, 0.5, 2, 4, 6, 7$. These sections include the regions at the entrance of the domain, after separation point, in the middle of the recirculation zone, after the reattachment point, after flow recovery, and finally, in the second corner of the bottom surface.
In Fig. 5.7, three contour plots for all grids topology are plotted to make comparison between cases. The influence of mesh resolution can be seen for each type of mesh. The last row of the figure shows the contours of the reference data. Although the streamwise velocity and pressure contours are very similar to each other, the difference in the kinetic energy contours are obvious and seems fine meshes including Sq_4, Tri_4, and $Poly_4$ have more similarity with reference data contours.
The flow pattern assessment is well illustrated by the contours plots of streamwise velocity and kinetic energy. Fig. 5.18 shows the contours of four main parameters applied for flow assessments. Inspection of velocity magnitude vector contour, Fig. 5.18a, reveals flow direction in every point of the domain. The flow circulation is clearly visible not only specified by the color but also vectors show the flow direction. Fig. 5.18b shows the turbulent kinetic energy contour. The high value of energy specified by yellow color which occurs immediately after separation point and has continued along with the domain. Although the turbulent kinetic energy depreciated in value, its influence on the channel flow is obvious.

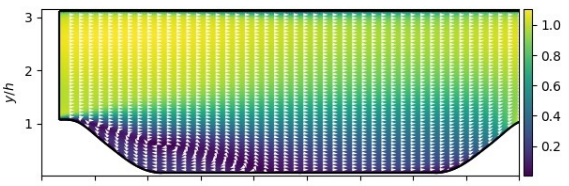

(a) Velocity magnitude vectors

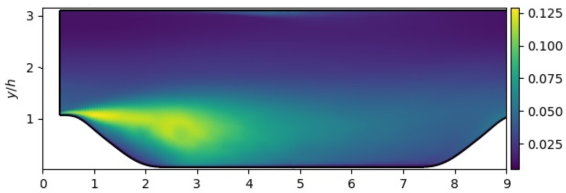

(b) Turbulent kinetic energy, <k>

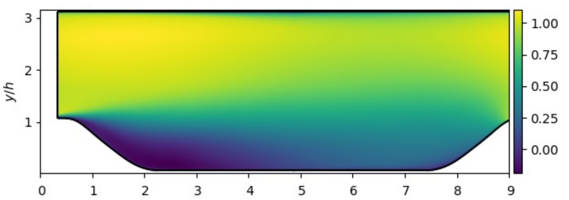

(c) Streamwise velocity, <u>

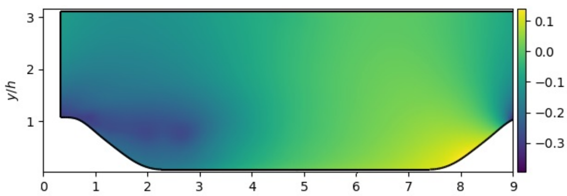

(d) Pressure, <p>

Figure 5.8: Contours of four main parameters applied for flow assessments.

Streamwise velocity contour shows high and low-velocity zones and specified them by yellow and blue colors, respectively (see Fig.5.18c). The velocity in the top half of the channel is larger than the lower area between two hill crest where the velocity has its minimum values. It is predicted that separation, recirculation, and reattachment points have a direct relation with velocity and pressure profiles. Fig.5.18d shows the pressure distribution contour in the channel and it can be seen that the pressure value increased in the second half of the domain and maximum pressure zone occur on the second hill ramp and closed to the wall.
Fig. 5.9 shows the mean velocity profiles in different zones for the domain with the

square mesh. Profiles include all grid sizes from coarsest, d_1, to the finest mesh, d_4. Looking at the profiles, all square mesh results slightly underestimate the peak velocity close to the bottom surface, but among all, Sq_3 has more agreement with the reference data. Close to the top wall, all cases have excellent agreement with reference data.

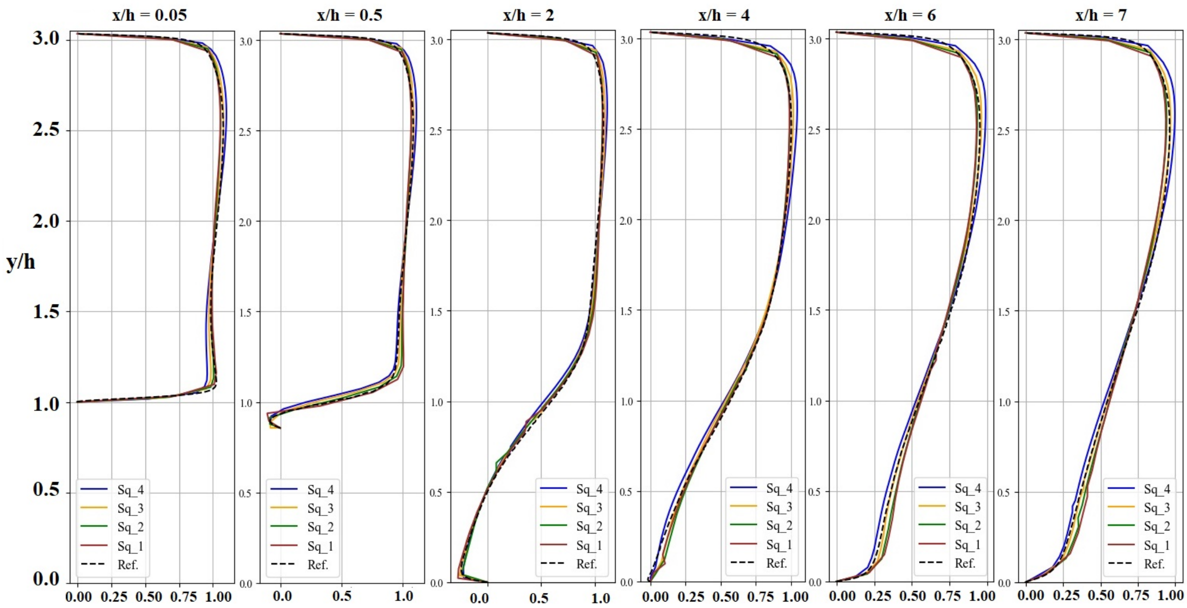

Figure 5.9: Streamwise velocity profiles along the hill at selected locations for all square grids.

Figure 5.10 shows the vertical velocity for the square meshes and shows a discrepancy between reference data and our cases. The most obvious difference is sharp edges in all square meshes which is absent in the reference data. At two first locations, $x/h = 0.05, 0.5$, there is a discrepancy between cases and reference data, while in the rest of the locations profiles are more agreement with the reference data. The finest square mesh, Sq_4, is extremely well reflected around the reattachment point. In general, the coarse mesh has less agreement and Sq_3 and Sq_4 are more agreement. The kinetic energy profile, Fig. 5.11, shows a relatively good agreement of the finest mesh, Sq_4, at almost all sections, while decreasing the grid resolution, the agreement declines.

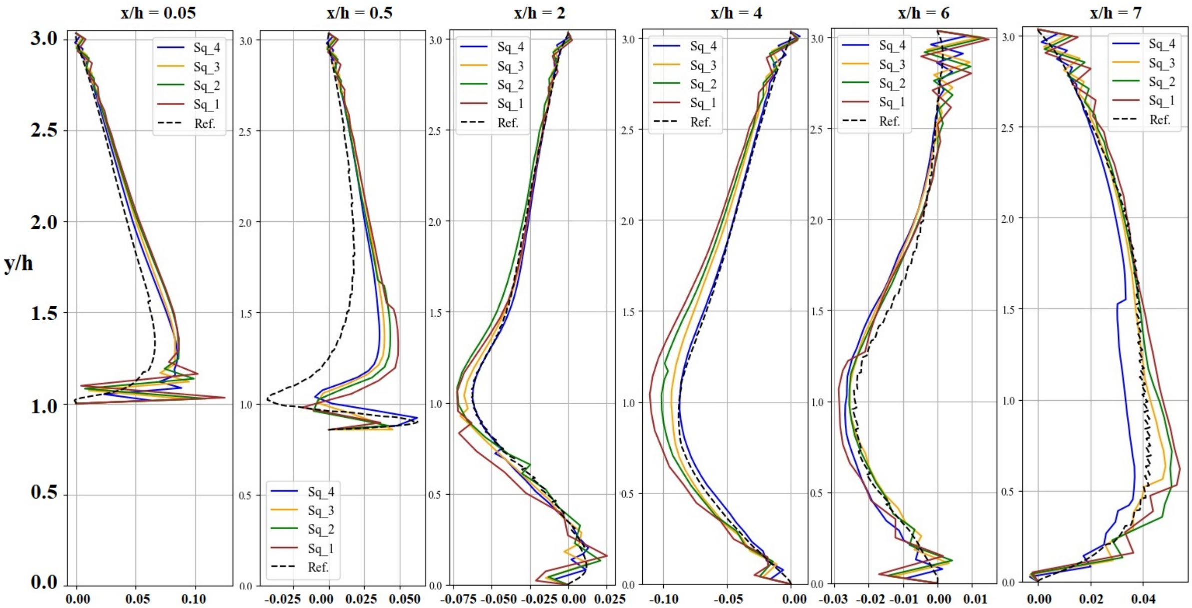

Figure 5.10: Vertical velocity profiles along the hill at selected locations for all square grids.

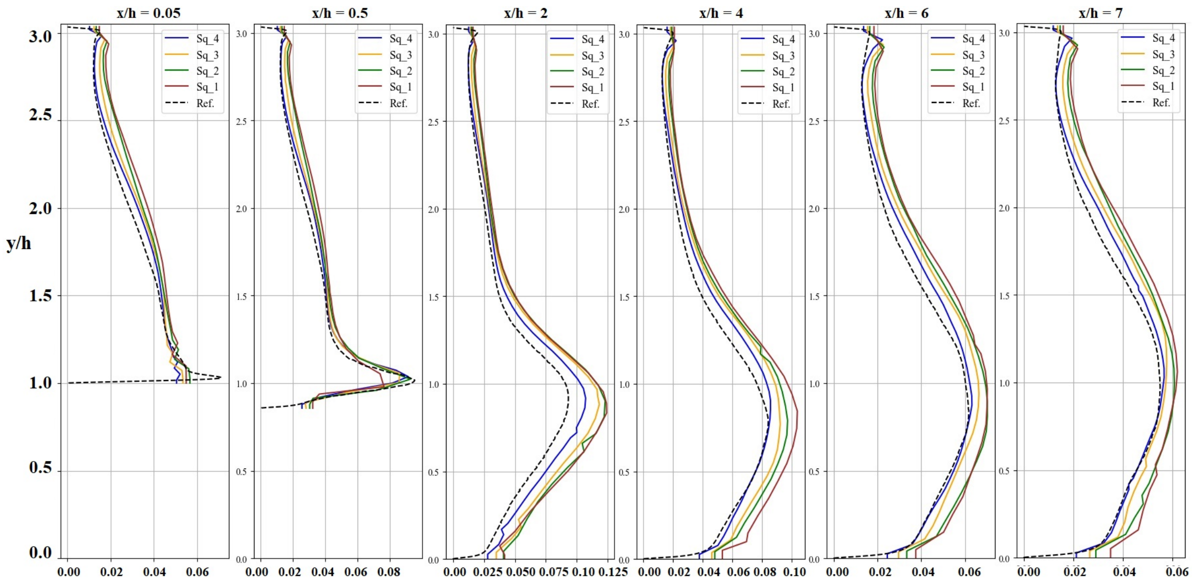

Figure 5.11: Kinetic energy profiles along the hill at selected locations for all square grids.

Figure 5.12 and 5.13 show the mean and vertical velocities for the domain with four different polygon grids. It can be seen that the most fine mesh, $Poly_4$, is very well-matched with reference data for almost all sections. Overall, polygon grids are more agreement with the reference data compared with the square grids.

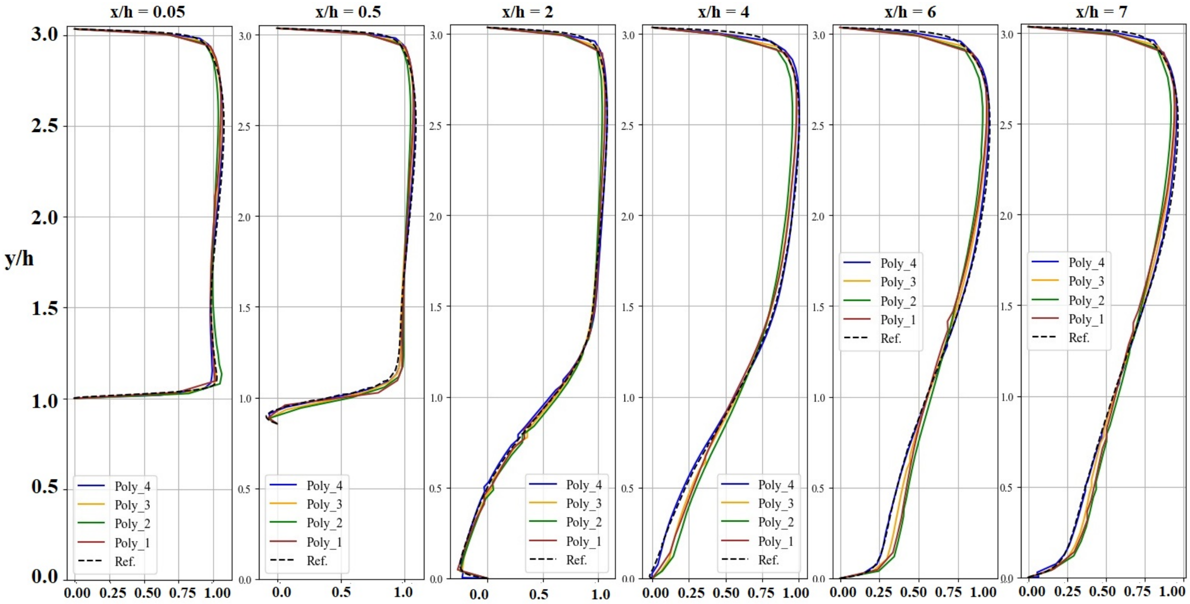

Figure 5.12: Streamwise velocity profiles along the hill at selected locations for all polygon grids.

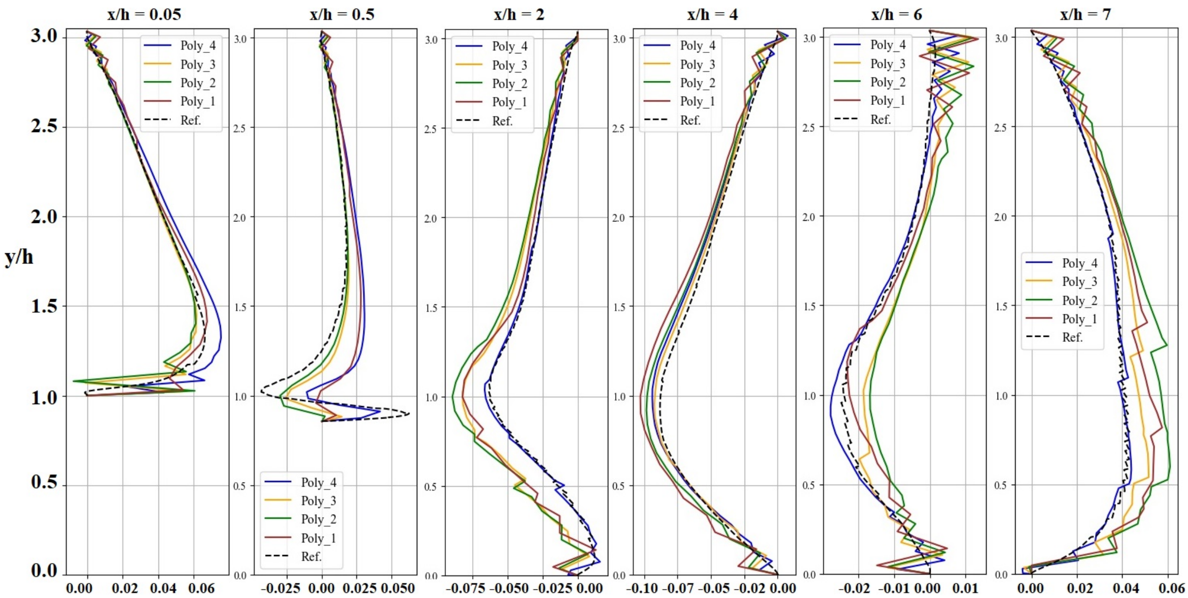

Figure 5.13: Vertical velocity profiles along the hill at selected locations for all polygon grids.

Fig. 5.14 shows the kinetic energy profile along the hill at selected locations for all polygon grids. All results slightly underestimate the peak kinetic energy close to the bottom wall, but the finest mesh result is much closer to the reference data. The kinetic energy close to the top wall also has a better agreement with the reference data.

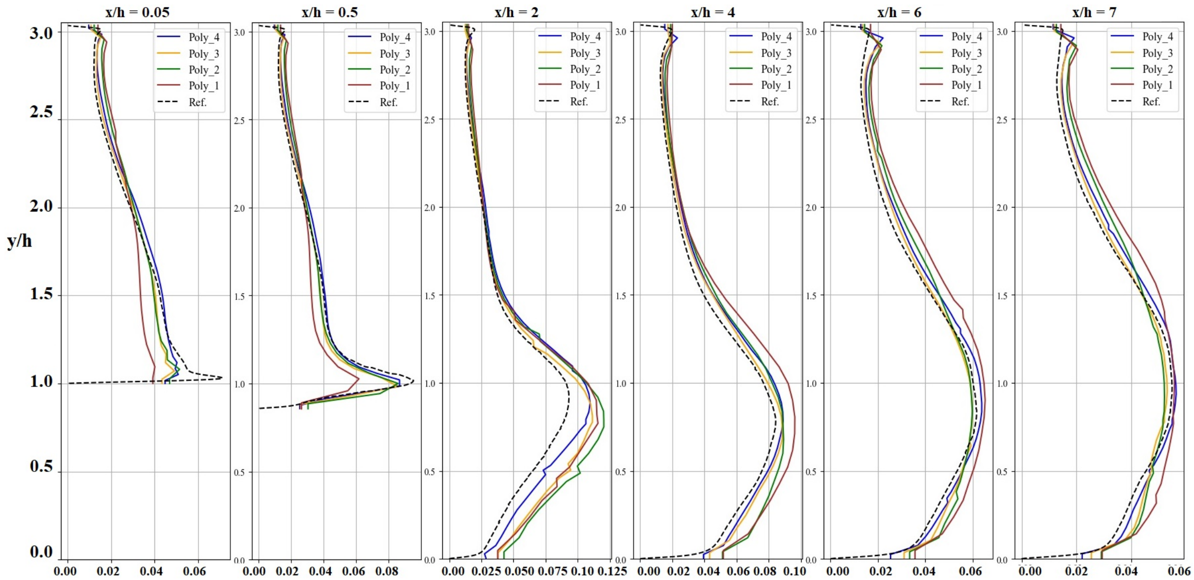

Figure 5.14: Kinetic energy profile along the hill at selected locations for all polygon grids.

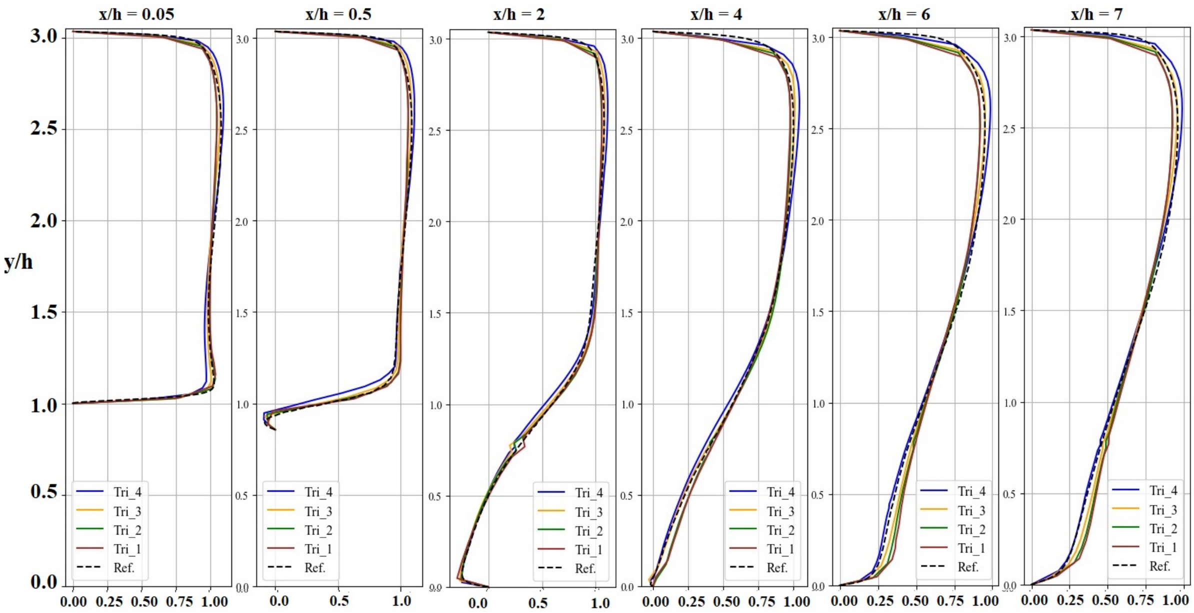

Figure 5.15: Streamwise velocity profiles along the hill at selected locations for all triangle grids.

Fig. 5.15 shows the streamwise velocity for the domain with a triangle mesh. Considering the first half of the domain, it can be seen that all grid sizes except the finest one, have a good agreement with the reference data, while in the second half of the domain the finest mesh is more close to the reference data. But in general, the case Tri_3, has a well-matched agreement at almost all sections. Fig. 5.16 shows the vertical velocity. Regarding profiles, at a close distance from the surface, there is a good agreement between the finest mesh and reference data, while far from the surface there is no specific trend for the profiles.

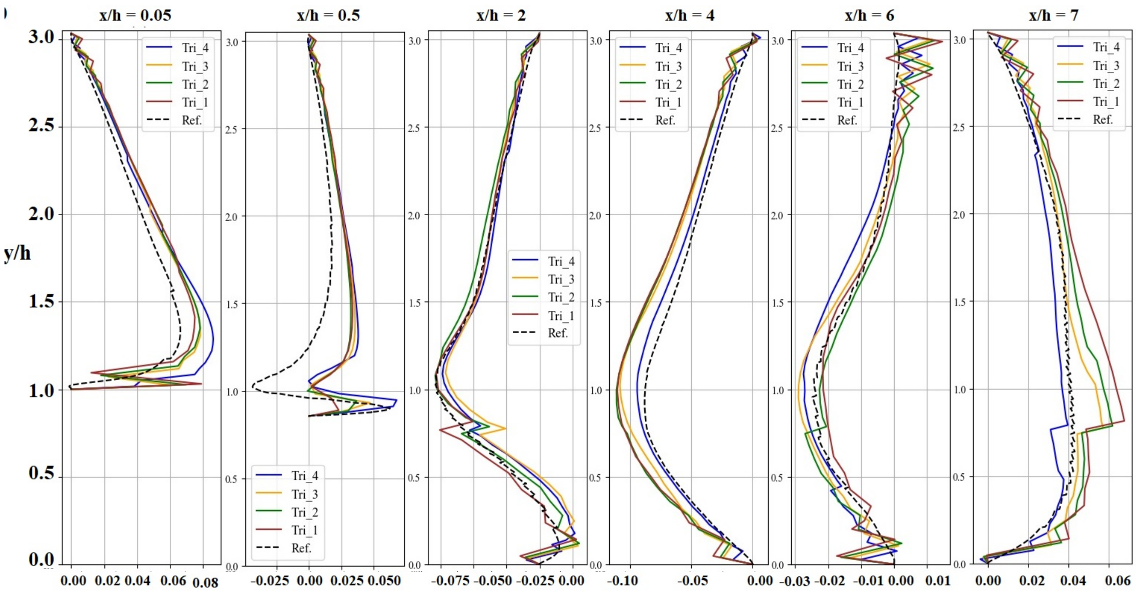

Figure 5.16: Vertical velocity profiles along the hill at selected locations for all triangle grids.

The kinetic energy profile for the domain with triangle grids is shown in Fig. 5.17. Although the results, depends on the profile, slightly overestimate at $x/h > 0.5$ and it can say the finest grid, Tri_4, is closer to the reference data. The profiles close to the top side are very similar to the reference data.

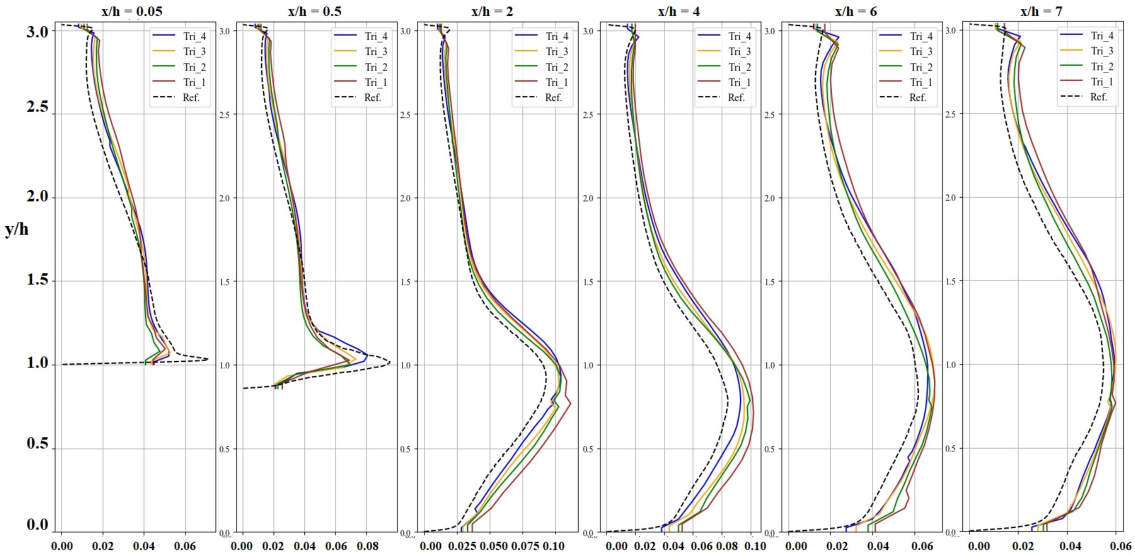

Figure 5.17: Kinetic energy profile along the hill at selected locations for all triangle grids.

Figure 5.18 shows a comparison between mean streamwise velocity, normal velocity, and turbulent kinetic energy profiles for all finest of three types of mesh with the reference data. Although polygon mesh is in better agreement with the reference data.

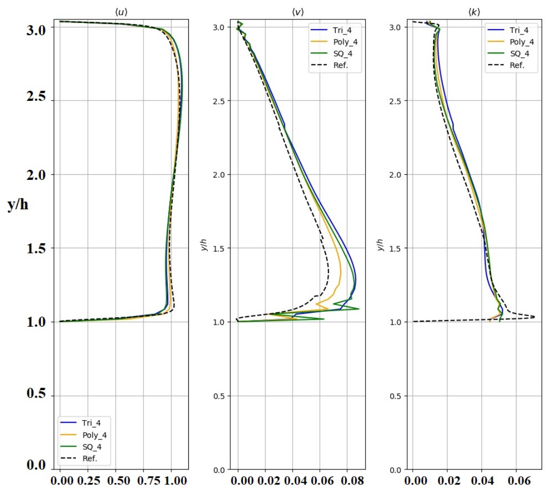

(a) Profiles at $x/h = 0.05$

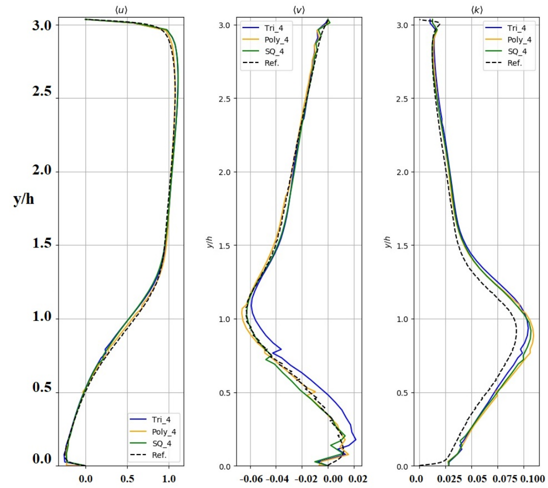

(b) Profiles at $x/h = 2$

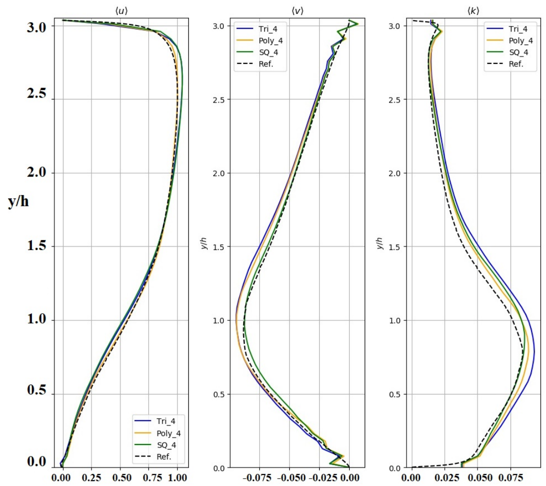

(c) Profiles at $x/h = 4$

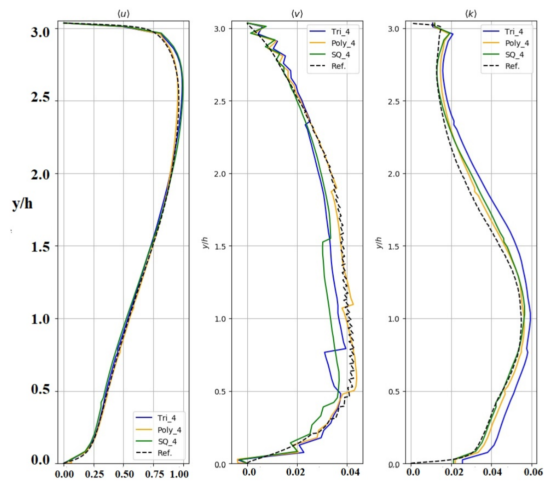

(d) Profiles at $x/h = 7$

Figure 5.18: Mean streamwise velocity, normal velocity, and turbulent kinetic energy profiles at $x/h = 0.05, 2, 4, 7$ for all three finest mesh.

5.3 Flow characteristics assessment

In order to find the certain locations of separation and reattachment points, simulation results of the twelve cases were post processed using the Python programming language. Figure 5.19 shows a close-up view of the domain with mesh resolution and locations of separation and reattachment points.

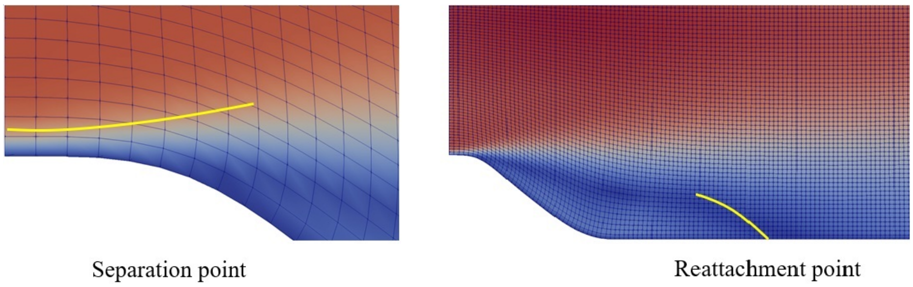

Figure 5.19: Close-up view of the separation and reattachment points.

Table 5.1 shows the separation and reattachment points for all cases and Fig. 5.20 shows the schematic of these points along the domain. The y-axis shows the cases in three types of mesh and four grid resolution for each. The x-axis length is as same as the domain and dashed lines illustrate the separation and reattachment points of reference data. Evidence shows a larger difference in the reattachment point in comparison with the separation point. Secondly, for each type of mesh, mesh with the highest resolution is closer to the reference data. In order to rank the candidates with a reasonable agreement with the reference data, the triangle mesh with high resolution, Tri_4, is the most compatible case with the reference data and $Poly_2$ has the weakest compatibility with the reference data.

Table 5.1: Separation and reattachment points.

Mesh Type	**Case name**	**separation point**	**reattachment point**
Triangle	Tri_4	0.28	4.2
	Tri_3	0.29	4.1
	Tri_2	0.29	3.9
	Tri_1	0.37	3.8
Polygon	$Poly_4$	0.30	4.0
	$Poly_3$	0.31	3.6
	$Poly_2$	0.28	3.6
	$Poly_1$	0.32	3.7
Square	Sq_4	0.28	4.0
	Sq_3	0.32	3.8
	Sq_2	0.28	3.8
	Sq_1	0.33	3.9

Table 5.2: Deviation's percentage of separation and reattachment points in compare with the reference data.

Mesh Type	Case name	Separation deviation(%)	Re-attachment deviation(%)
Triangle	Tri_4	20	6
	Tri_3	17	8
	Tri_2	16	11
	Tri_1	6	14
Polygon	$Poly_4$	13	10.5
	$Poly_3$	12	18
	$Poly_2$	20	19
	$Poly_1$	8	16
Square	Sq_4	20	11
	Sq_3	8	13
	Sq_2	19	15
	Sq_1	5	13

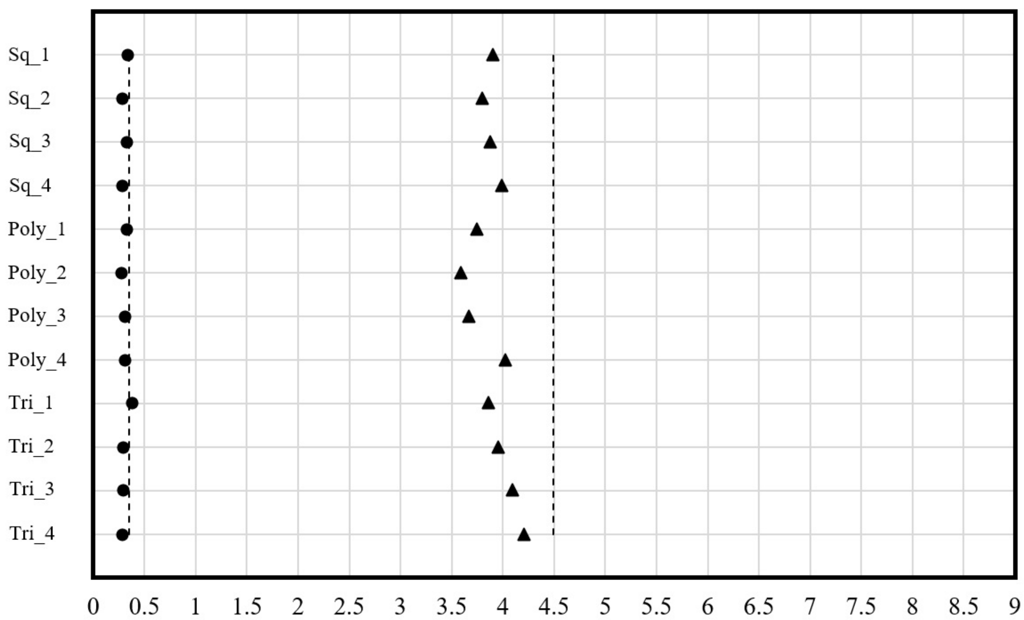

Figure 5.20: Separation and reattachment points for cases with different mesh topologies.

The separation and reattachment points in cases include Tri_2, $Poly_4$, and Sq_4 , which seems occur in the same location and have reasonable agreement with the reference data, while two first coarse square meshes, Sq_1 and Sq_2, have less agreement with the reference data. In general, it seems that triangle and polygon meshes are the best and worst grid candidates for the simulation, respectively.

6

Conclusions and Future Works

6.1 Conclusion

An investigation has been conducted on the performance of wall-modelled LES method on unstructured grids when applied to a separated flow in a periodic hill. The most distinctive feature of this study is evaluation of the influence of grid topology and mesh resolution on the accuracy of separation and reattachment points, the wall-shear stress coefficient, the pressure coefficient, and velocity profiles. The statistical data elicited from the study illustrate a noticeable influence of grid topology on the results and prove that meshing strategy plays a key role in accurate prediction. While results of this research demonstrate many familiar flow behavior, they also reveal a number of engaging results. The overall conclusions of this analysis can be summarized as follows.

- The flow over periodically arranged hills is investigated. The geometry has a specific configuration to study a flow separating from a curved surface which makes it well suited as a benchmark case for computing separated flows.
- Wall-Modelled Large Eddy Simulations on three different grid typologies have been conducted. It was shown that WMLES predict the flow features accurately.
- Results show that unstructured grids are not worse that structured grids. In general, the results show reasonable accuracy with reference data even on coarse grids.
- Simulation results illustrated a noticeable distinction in sensitivity between separation and reattachment points. Regarding this, the reattachment point is highly sensitive to mesh topology.
- The results show that, even if the wall model does not predict the correct temporal evolution of the wall friction, we can still capture the non-equilibrium effects in the velocity profile. This means that, in this particular case, the errors in the friction are not directly propagated back into the velocity profile.
- The results highlighted sensitivity of the WMLES method on the grid topology. Square, polygon, and triangle meshes are three candidates in this study and the results show a noticeable changes in flow feature profiles. Fig. 5.20 shows that the influence of mesh topology on the separation and reattachment points. In terms of compatibility of the results with the reference data, triangle mesh achieved the more compatible result with a minimum deviation of 5% for finest mesh, Tri_4, and a maximum deviation of 10% for the coarsest mesh, Tri_1. Polygon mesh ranked second with minimum and maximum deviation of 10.5%

and 16.6%, respectively.Finally, the polygon mesh with minimum 10.5% and maximum 19% deviation from the reference data has the least compatibility. However, for some cases, mostly in for square and polygon mesh, there are two exceptional cases include Sq_1 and $Poly_1$ which are more agreement compare with the finer mesh.

6.2 Possible future works

6.2.1 Proposal 1

The current work investigated the performance of WMLES on unstructured grids. All simulations have been performed in a certain Reynolds number, $Re = 10595$, based on the hill height and the bulk velocity. The idea for the future work can be defined in such a way that a range of Reynolds numbers, particularly high Re, for the same domain.

6.2.2 Proposal 2

The current computational domain is a periodic hill with fully turbulent flow. It is highly interesting to assess the accuracy of the results close to the wall. On the other hand, there is numerous subgrid-scale modelling for a turbulent flow. The aim of this work is to propose to compare different SGS models for the same domains. For instance, the performance of wall-adapting local eddy viscosity (WALE) model, the Dynamic Smagorinsky model (DSM) and the Coherent Structures model (CSM) can be investigated for a range of Reynolds number.

Bibliography

[1] Larsson, J., Kawai, S., Bodart, J., Bermejo, I., *Large eddy simulation with modeled wall-stress: recent progress and future directions* Mechanical Engineering Reviews, 2015.

[2] Gloerfelt, X., Cinnella, P., *Large Eddy Simulation Requirements for the Flow over Periodic Hills* Netherlands, Delft University of Technology, 2019.

[3] Mukha, T., Bensow, R.E., Liefvendahl, M., *Predictive Accuracy of Wall-Modelled Large-Eddy Simulation on Unstructured Grids*, Chalmers University of Technology, Department of Mechanics and Maritime Sciences.

[4] Krank, B., Kronbichler, M., Wall, W., *Wall modeling via function enrichment: extension to detached-eddy simulation* Institute for Computational Mechanics, Technical University of Munich, Germany, 2017.

[5] Lodato, G., Castonguay, P., Jameson, A., *Structural Wall-modeled LES Using a High-order Spectral Difference Scheme for Unstructured Meshes*, Flow Turbulence Combust, 579–606, 2014.

[6] Fröhlich, J., Mellen, C., Rodi, W., Temmerman, L., *Highly resolved large-eddy simulation of separated flow in a channel with streamwise periodic constriction*, Journal of Fluid Mechanics 526:19 - 66, 2005.

[7] Almeida, G.P., Durao, D.F.G., Heitor, M.V., *Wake flows behind two-dimensional model hills*, Exp Thermal Fluid Sci 1993;7:87–101.

[8] Mellen, C.P., Fröhlich, J., Rodi, W., Deville, M., Owens, R., *Large-eddy simulation of the flow over periodic hills*, Proceedings of 16th IMACS world congress, Lausanne, Switzerland. CD-ROM; 2000.

[9] Almeida,G.P., Durão, D.F.G., Heitor, M.V., *Wake flows behind two-dimensional model hills*, Journal of Experimental Thermal and Fluid Science Volume 7, Issue 1, July 1993, Pages 87-101.

[10] Breuer, M., Peller, N., Rapp, C.H., Manhart, M., *Flow over periodic hills – Numerical and experimental study in a wide range of Reynolds numbers*,

Journal of Computers Fluids Volume 38, Issue 2, February 2009, Pages 433-457.

[11] W. Gao, W Zhang, W. Cheng, R. Samtaney *Wall-modelled large-eddy simulation of turbulent flow past airfoils*, J. Fluid Mech. (2019), vol. 873, pp. 174–210.

[12] Sadrehaghighi, I., *Mesh Generation in CFD*, CFD Open Series, Patch 1.86.7.

[13] https://wmles.umd.edu/hybrid-les-rans-models/.

[14] https://turbmodels.larc.nasa.gov/Other_LES_Data/2dhill_periodic.html.

[15] Frohlich, J., Rodi, W., *Introduction to Large Eddy Simulation of Turbulent Flow*, https://tu-dresden.de/ing/maschinenwesen/ism/psm/ressourcen/dateien/mitarbeiter/froehlich/publications/Froehlich_Rodi_Cambridge_2002.pdf?lang=en.

[16] Garnier, E., Sagaut, P., Adams, N., *LES Governing Equations*, https://www.researchgate.net/publication/251261479.

[17] Balakumar, P., Mellen, G., Pierce, B., *DNS, LES, and wall-modeled LES of separating flow over periodic hills*, Center for Turbulence Research, Proceedings of the Summer Program, 2014.

[18] Boudier, G., Staffelbach, G., Gicquel, M., Poinsot, T., *Mesh Dependency of Turbulent Reacting Large-Eddy Simulations of a Gas Turbine Combustion Chamber*, Quality and Reliability of Large-Eddy Simulations. Ercoftac Series, vol 12. Springer, pp 319-330, 2008.

[19] Spalding.D.B., *A single formula for the of the wall*, Journal of Applied Mechanics, vol28. 455-458, 1961.

[20] Ben-Nasr, G., Hadjadj, A., Chaudhuri, A., Shadloo, M.S., *Assessment of subgrid-scale modeling for large-eddy simulation of a spatially-evolving compressible turbulent boundary layer*, Journal of Computers and Fluids, 151, 144-158, 2017.

[21] *OpenFOAM: User Guide v2006, The open source CFD toolbox*, https://www.openfoam.com/documentation/guides

[22] Eberhardt, S., Hickel, S., *Large-Eddy Simulation of a Scramjet Strut Injector with Pilot Injection* Netherlands, Delft University of Technology, 2016.

A

Appendix 1

A.1 CAD Geometry Data

The first step to create a computational domain is creating the domain with an accurate CAD design. In the present work, all CAD data prepared from the Almeida work [9] and NASA Langley Research Center [14]. Follow, you can find data include the general dimension in x, y, and z directions as well as domain boundary's point.

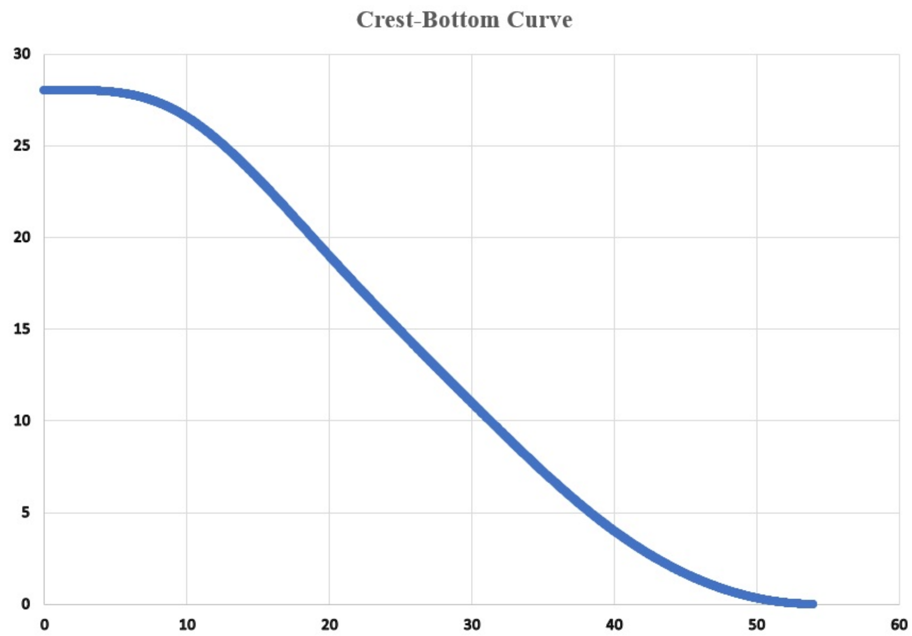

Figure A.1: Hill's crest to domain's bottom curve in an Excel sheet.

Fig.A.1 shows the hill's crest to domain's bottom curve in an Excel sheet. Note that, there is an availability to import Excel sheet data directly to the SOLIDWORK software. In order to create the flat parts of the domain such as top, bottom, inlet, outlet, left, and right walls, boundaries lines generated based on NASA data[14] and then merged to the curved lines.

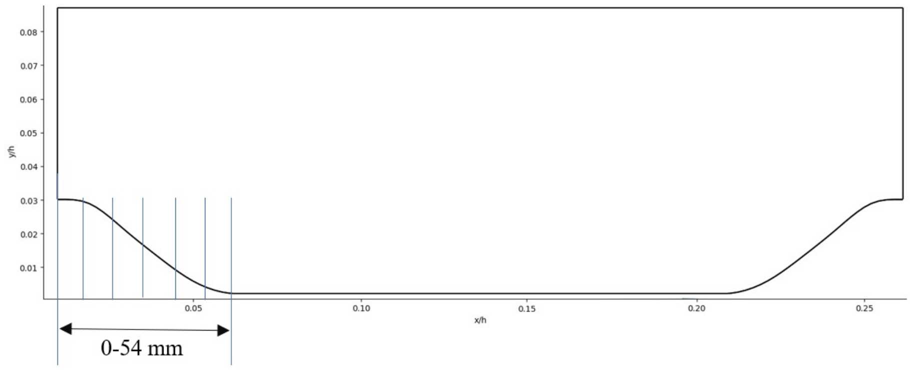

Figure A.2: Curve surface sections.

Table A.1: Spline section's location in CAD design

0.0	28.0
9.0	27.0
14.0	24.0
20.0	19.0
30.0	11.0
40.0	4.0
54.0	0.0

Based on NASA 2D periodic hill, follow are the relations to find the height (mm), h, along the domain. Fig. A.2 shows the sections along the curved surface of the periodic hill.

Between x=0. and x=9.
h(x)=min(28., 2.800000000000E^{+01}+0.000000000000$E^{00}*x$+6.775070969851$E^{-3}*x^2$ $- 2.124527775800E^{-03} * x^3$)

Between x=9. and x=14.
h(x)= 2.507355893131E^{+01} $+ 9.754803562315E^{-01} * x - 1.016116352781E^{-01} * x^2$ $+ 1.889794677828E^{-03} * x^3$

Between x=14. and x=20.
h(x)= 2.579601052357E^{+01} $+ 8.206693007457E - 01 * x - 9.055370274339E - 02 * x^2$ $+ 1.626510569859E - 03 * x^3$

Between x=20. and x=30.
h(x)= 4.046435022819E^{+01} $- 1.379581654948E^{+00} * x + 1.945884504128E^{+02} * x^2$ $- 2.070318932190E^{-04} * x^3$

Between x=30. and x=40.
h(x)= 1.792461334664E^{+01} $+ 8.743920332081E^{-01} * x - 5.567361123058E^{-02} * x^2$ $+ 6.277731764683E^{-04} * x^3$

Between x=40. and x=54.
h(x)=max(0., 5.639011190988E$^{+01}-2.010520359035E^{+00}*x1.644919857549E^{-02}*x^2$
$+ 2.674976141766E - 05 * x^3$)

In the LES, the geometry has been nondimensionalized so that the hill height is 1.